5-2015

A Slow Neutron Polarimeter for the Measurement of Parity-Odd Neutron Rotary Power

W. M. Snow
Indiana University - Bloomington

E. Anderson
Indiana University - Bloomington

L. Barron-Palos
Universidad Nacional Autónoma de México

See next page for additional authors

Snow, W.M., E. Anderson, L. Barrón-Palos, C. D. Bass, T. D. Bass, B. E. Crawford, C. Crawford, J. M. Dawkins, D. Esposito, J. Fry, H. Gardiner, K. Gan, C. Haddock, B. R. Heckel, A. T. Holley, J. C. Horton, C. Huffer, J. Lieffers, D. Luo, M. Maldonado-Velázquez, D. M. Markoff, A. M. Micherdzinska, H. P. Mumm, J. S. Nico, M. Sarsour, S. Santra, E. I. Sharapov, H. E. Swanson, S. B. Walbridge and V. Zhumabekova. "A Slow Neutron Polarimeter for the Measurement of Parity-Odd Neutron Rotary Power." Review of Scientific Instruments 86.5 (May 2015), 055101.

A Slow Neutron Polarimeter for the Measurement of Parity-Odd Neutron Rotary Power

Abstract
We present the design, description, calibration procedure, and an analysis of systematic effects for an apparatus designed to measure the rotation of the plane of polarization of a transversely polarized slow neutron beam as it passes through unpolarized matter. This device is the neutronoptical equivalent of a crossed polarizer/analyzer pair familiar from light optics. This apparatus has been used to search for parity violation in the interaction of polarized slow neutrons in matter. Given the brightness of existing slow neutron sources, this apparatus is capable ofmeasuring a neutron rotary power of $d\phi/dz = 1 \times 10^{-7}$ rad/m.

Keywords
Neutrons, Magnetic Fields, Rotation Measurement, Liquid Helium, Error Analysis

Disciplines
Atomic, Molecular and Optical Physics | Physics

Authors
W. M. Snow, E. Anderson, L. Barron-Palos, C. D. Bass, T. D. Bass, Bret E. Crawford, C. Crawford, J. M. Dawkins, D. Esposito, J. Fry, H. Gardiner, K. Gan, C. Haddock, B. R. Heckel, A. T. Holley, J. C. Horton, C. Huffer, J. Lieffers, D. Luo, M. Maldonado-Velazquez, D. M. Markoff, A. M. Micherdzinska, H. P. Mumm, J. S. Nico, M. Sarsour, S. Santra, E. I. Sharapov, H. E. Swanson, S. B. Walbridge, and V. Zhumabekova

REVIEW OF SCIENTIFIC INSTRUMENTS **86**, 055101 (2015)

A slow neutron polarimeter for the measurement of parity-odd neutron rotary power

W. M. Snow,[1] E. Anderson,[1] L. Barrón-Palos,[2] C. D. Bass,[3] T. D. Bass,[1] B. E. Crawford,[4] C. Crawford,[5] J. M. Dawkins,[1] D. Esposito,[6] J. Fry,[1] H. Gardiner,[7] K. Gan,[8] C. Haddock,[1] B. R. Heckel,[9] A. T. Holley,[10] J. C. Horton,[1] C. Huffer,[11] J. Lieffers,[12] D. Luo,[1] M. Maldonado-Velázquez,[2] D. M. Markoff,[13] A. M. Micherdzinska,[1] H. P. Mumm,[14] J. S. Nico,[14] M. Sarsour,[15] S. Santra,[16] E. I. Sharapov,[17] H. E. Swanson,[9,a)] S. B. Walbridge,[1] and V. Zhumabekova[18]

[1]*Indiana University and Center for the Exploration of Energy and Matter, 2401 Milo B. Sampson Lane, Bloomington, Indiana 47408, USA*
[2]*Instituto de Física, Universidad Nacional Autónoma de México, Ciudad de México, D.F. 04510, México*
[3]*LeMoyne College, 1419 Salt Springs Road, Syracuse, New York 13214, USA*
[4]*Gettysburg College, 300 North Washington Street, Gettysburg, Pennsylvania 17325, USA*
[5]*University of Kentucky, 177 Chem.-Phys. Building, 505 Rose Street, Lexington, Kentucky 40506-0055, USA*
[6]*University of Dayton, 300 College Park, Dayton, Ohio 45469, USA*
[7]*Louisiana State University, Baton Rouge, Louisiana 70803, USA*
[8]*The George Washington University, 2121 I Street N.W., Washington, District of Columbia 20052, USA*
[9]*University of Washington/Center for Experimental Nuclear Physics and Astrophysics, Box 354290, Seattle, Washington 98195, USA*
[10]*Tennessee Tech University, 1 William L. Jones Drive, Cookeville, Tennessee 38505, USA*
[11]*North Carolina State University, 2401 Stinson Drive, Raleigh, North Carolina 27695, USA*
[12]*Embry-Riddle Aeronautical University, 600 South Clyde Morris Blvd., Daytona Beach, Florida 32114, USA*
[13]*North Carolina Central University/Triangle Universities Nuclear Lab, 1801 Fayetteville Street, Durham, North Carolina 27707, USA*
[14]*National Institute of Standards and Technology, 100 Bureau Drive, Gaithersburg, Maryland 20899, USA*
[15]*Georgia State University, 29 Peachtree Center Avenue, Atlanta, Georgia 30303-4106, USA*
[16]*Bhabha Atomic Research Centre, Trombay, Mumbai 400 085, India*
[17]*Joint Institute for Nuclear Research, Joliot-Curie 6, 141980 Dubna, Russia*
[18]*Al-Farabi Kazakh National University, Al-Farabi Ave. 71, 050038 Almaty, Kazakhstan*

(Received 1 December 2014; accepted 19 April 2015; published online 5 May 2015)

We present the design, description, calibration procedure, and an analysis of systematic effects for an apparatus designed to measure the rotation of the plane of polarization of a transversely polarized slow neutron beam as it passes through unpolarized matter. This device is the neutron optical equivalent of a crossed polarizer/analyzer pair familiar from light optics. This apparatus has been used to search for parity violation in the interaction of polarized slow neutrons in matter. Given the brightness of existing slow neutron sources, this apparatus is capable of measuring a neutron rotary power of $d\phi/dz = 1 \times 10^{-7}$ rad/m. © *2015 AIP Publishing LLC.* [http://dx.doi.org/10.1063/1.4919412]

I. INTRODUCTION

Measurements of the rotation of the plane of polarization of particles as they move through matter are employed in many areas of physics.[1] The oldest and still most common example is the rotation of the plane of polarization of light as it passes through an optically active medium. In light optics, such optical activity is expressed as the change of the rotation angle per unit length $d\phi/dz$ and is referred to as the rotary power of the medium. The motion of the polarization vector of the particle relative to its momentum through the medium can be pictured as a corkscrew motion in space. The handedness of a corkscrew is changed upon a mirror reflection or a parity transformation. A measurement of the rotary power is therefore typically used to access some property either of the medium or the interaction of the particle with the medium which violates mirror symmetry. Common examples in light optics include the handedness of molecular structures and certain types of ordering in magnetic materials.

Like light, neutrons can be polarized and can pass through macroscopic amounts of matter due to their electrical neutrality. It is therefore possible to measure the neutron rotary power of condensed matter.[2,3] Furthermore, neutrons with energies in the meV range are slow enough to possess largely elastic interactions with matter and can therefore be manipulated using neutron optical components in ways analogous to light optics. However, there are a few interesting differences. One fundamental difference is that the neutron is a massive spin 1/2 particle, whereas the photon is a massless spin 1 particle. Although the quantum mechanical base states for the spin degrees of freedom in both cases possesses two independent components, the angles which appear in the quantum mechanical rotation operators describing these particles differ by a factor of 2. Another more practical difference is that the

a)Author to whom correspondence should be addressed. Electronic mail: swanson@npl.washington.edu

magnetic moment of the neutron is strongly influenced by the external magnetic field of the earth. It is difficult to suppress the earth's magnetic field enough to completely eliminate the rotation of the neutron spin in the residual fields, and so, special measurement methods must be employed to remove this large background effect. Similar considerations would apply to attempts to measure the rotary power of polarized electrons in matter. Such measurements were proposed[4] but to our knowledge not yet realized.

In this paper, we describe an apparatus capable of measuring the parity-odd component of the neutron rotary power in a medium. A statistical sensitivity of $d\phi/dz = 1 \times 10^{-6}$ rad/m with a systematic uncertainty of $d\phi/dz = 1 \times 10^{-7}$ rad/m was achieved in a recent effort to search for neutron spin rotation from the weak interaction between the neutron and ^{4}He nuclei in a liquid helium target.[5] The results from this experiment have been used to set stringent limits for possible exotic parity-odd interactions of the neutron in matter which could come from vector boson exchange[6] or torsion,[7] and a similar apparatus is under construction for a more sensitive measurement in liquid helium.[8] Given the intensity of present and planned slow neutron beams, statistical sensitivities of $d\phi/dz = 1 \times 10^{-7}$ rad/m and higher are within reach in the foreseeable future, requiring even further reduction in systematic uncertainties. Much of this paper emphasizes the strategies used to determine or bound the size of these systematic uncertainties.

Our apparatus must distinguish small parity-odd rotations of polarized slow neutrons from rotations that arise from magnetic fields. We will use this experimental apparatus as an illustration of an instrument which can be easily adapted for other target media. A very similar design for measuring slow neutron weak rotary power was employed for the first time in a series of measurements which observed parity violation in nuclei such as ^{117}Sn,[9] Pb,[10] and ^{139}La[11] and sought for effects in ^{133}Cs, Rb, and ^{81}Br.[12] Experiments to measure parity-odd spin rotation on resonances in atomic[13] and nuclear systems, including neutron spin rotation of epithermal neutrons passing through nuclear targets possessing compound nuclear resonances,[14–17] have also been described in the literature. Brief descriptions of the experimental technique and apparatus to measure slow neutron spin rotation have appeared[5,18–20] and an extensive discussion of an earlier version of this apparatus appears in a Ph.D. thesis,[21] but to our knowledge, a full description of an apparatus to measure parity-odd neutron rotary power with high sensitivity using slow neutrons has not appeared before in the scientific literature.

The paper is organized as follows. In Sec. II, we review the theory of parity violation in neutron optics and show how to measure the rotation angle using a crossed polarizer/analyzer pair for a nonrelativistic spin 1/2 particle like the neutron. In Sec. III, we present a description of the apparatus. In Sec. IV, we describe how the neutron polarimeter is calibrated, including the use of the polarized neutrons themselves as a magnetometer. In Sec. V, we outline how to achieve a measurement limited by neutron counting statistics in the presence of nonstatistical noise from the neutron source. In Sec. VI, we outline the sources of systematic uncertainty. We offer our conclusions in Sec. VII.

II. THEORY OF PARITY VIOLATION IN NEUTRON OPTICS

A. Phenomenology

In this section, we review the relationship between parity-odd interactions of low energy neutrons and the phenomenon of parity-odd neutron spin rotation in neutron optics. We concentrate on neutrons with momenta that satisfy $kR \ll 1$, where k is the neutron wave vector and R is the range of the strong neutron-nucleus interaction. In this limit, the scattering amplitude $f(\theta)$ is predominantly s-wave,[22]

$$f(\theta) = f(0) = -a, \tag{1}$$

where a is the scattering length. Assume the neutron moves in a uniform medium of scatterers and consider the forward scattering limit. In this regime, the forward amplitude for the neutron motion obeys the Schrödinger equation with a optical potential,[23,24]

$$V_{opt} = \left(\frac{2\pi\rho\hbar^2}{m}\right) a, \tag{2}$$

where ρ is the number density of the scatterers in the medium and a is the scattering length defined in Eq. (1).

The wave equation inside the medium is

$$[\nabla^2 + {k_o}^2 n^2]\langle\psi_n\rangle = 0, \tag{3}$$

where $\langle\psi_n\rangle$ is the "coherent wave" or the forward scattering amplitude of the neutron in the medium, and we have defined the index of refraction n in the usual way,

$$n^2 = \frac{{k_i}^2}{{k_o}^2} = \left(1 - \frac{V + iW}{E}\right), \tag{4}$$

where V and W are the real and imaginary parts of the optical potential, and k_i and k_0 are the neutron wave vectors inside and outside the medium,

$${k_i}^2 = \frac{2m}{\hbar^2}(E - (V + iW)), \tag{5}$$

$${k_o}^2 = \frac{2mE}{\hbar^2}. \tag{6}$$

The index of refraction n can also be expressed in terms of the scattering amplitude a,

$$n = 1 - \frac{2\pi\rho a}{k^2} = 1 + \left(\frac{2\pi}{k^2}\right)\rho f(0). \tag{7}$$

The form of the coherent wave which satisfies Eq. (3) is

$$\langle\psi_n\rangle \sim e^{i\vec{k}\cdot\vec{r}} \sim e^{ink_o\cdot\vec{z}} \sim e^{-Im(n)\vec{k_o}\cdot\vec{z}} e^{iRe(n)\vec{k_o}\cdot\vec{z}}, \tag{8}$$

where the imaginary part of the potential W accounts for scattering and absorption processes which cause the wave to be attenuated as it passes through the medium. The real part of the potential contributes a phase shift to the neutron as it travels through the medium, given by

$$\varphi = Re(n)k_o z \tag{9}$$

for $\vec{k_o} = k_o\hat{z}$, where $\hat{z}$ is the incident neutron direction.

Now, we add in the effects of a parity-odd neutron interaction with the particles in the medium. In this case, the forward

scattering amplitude possesses both a parity-conserving (PC) s-wave component and a parity-violating (PV) p-wave component,

$$f(0) = f_{PC} + f_{PV}(\vec{\sigma}_n \cdot \vec{k}_n), \tag{10}$$

which results in two different scattering amplitudes, $f_\pm$, for the two opposite helicity states of the neutron $\vec{\sigma}_n \cdot \vec{k}_n = \pm k$. We label the two neutron helicity states $|+\rangle$ and $|-\rangle$, respectively. As a result, the two helicity states have different indices of refraction, n_+ and n_-, which accumulate different phase shifts as the neutron propagates through the medium. We combine Eqs. (9), (7), and (10) to obtain an expression for the two phases and identify the PC and PV terms,

$$\varphi_\pm = \varphi_{PC} \pm \varphi_{PV}, \tag{11}$$

where

$$\varphi_{PC} = kz\left(1 + \frac{2\pi\rho}{k^2} f_{PC}\right) \tag{12}$$

and

$$\varphi_{PV} = 2\pi\rho z f_{PV}. \tag{13}$$

In the absence of any neutron energy dependence in f_{PV} from resonances in the neutron scattering amplitude associated with the particles in the medium, the PV contribution to the phase is independent of neutron energy and directly proportional to the parity-odd part of the forward scattering amplitude.[2,3] This result contrasts sharply with the energy dependence of the parity-odd component of the rotary power near a resonance, which possesses a dispersive shape and goes to zero near the center of the resonance. The absence of a clear energy dependence to the parity-odd rotary power in the absence of resonances greatly increases the measurement difficulty.

The PV contribution to the forward scattering amplitude causes a rotation of the plane of polarization of the neutron through the different phases accumulated by the two helicity states in the medium. For a spin state transverse to the neutron momentum $|\uparrow\rangle$, which is a linear combination of equal amplitude contributions from the two helicity states,

$$|\uparrow\rangle = \frac{1}{\sqrt{2}}(|+\rangle + |-\rangle) \rightarrow \frac{1}{\sqrt{2}}(e^{i\varphi_+}|+\rangle + e^{i\varphi_-}|-\rangle). \tag{14}$$

So while the PC forward scattering contributes an unobservable overall phase factor which does not affect the spin state of the coherent wave, the PV forward scattering contributes an equal and opposite phase to the two helicity states. The PV rotation angle of the transverse spin, φ_{PV}, is therefore the accumulated difference in phase between the two helicity states,

$$\phi_{PV} = \varphi_+ - \varphi_- = 2\varphi_{PV} = 4\pi\rho z f_{PV}, \tag{15}$$

and we define the rotary power as in light optics as the change of the rotation angle per unit length $d\phi/dz = 4\pi\rho f_{PV}$.

The PV rotation angle is measured by comparing the intensities through a polarization analyzer set to transmit the $+\hat{y}$ and $-\hat{y}$ directions. Consider the case of a pure neutron spin state. The new state of the rotated state vector is given by

$$|\varphi\rangle = \frac{1}{\sqrt{2}}(e^{\frac{i\varphi}{2}}|+\rangle + e^{-\frac{i\varphi}{2}}|-\rangle), \tag{16}$$

where $\varphi = \phi_{PV}$. The expression for the spin up state along the analyzer direction $+\hat{y}$, which is transverse to both the momentum and the initial polarization, is given by a 90° rotation of the $\hat{x}$ state about the z axis,

$$|+\hat{y}\rangle = \frac{1}{2}[(1-i)|+\rangle + (1+i)|-\rangle], \tag{17}$$

and the neutron transmission intensity through the analyzer set in the $+\hat{y}$ direction is thus given by

$$N_+ = |\langle +\hat{y}|\varphi\rangle|^2 = \frac{1}{2}(1 + \sin\phi_{PV}). \tag{18}$$

Similarly, the count rate for the $-\hat{y}$ state is

$$N_- = \frac{1}{2}(1 - \sin\phi_{PV}). \tag{19}$$

So, the rotation angle of the spin about the momentum axis is

$$\sin\phi_{PV} = \frac{N_+ - N_-}{N_+ + N_-}. \tag{20}$$

The neutron spin rotation angle is therefore obtained by measuring the intensities of neutrons transmitted through a crossed polarizer ($\hat{x}$) and analyzer ($\hat{y}$) system in which the final analyzer direction alternates between $+\hat{y}$ and $-\hat{y}$. For the small angles encountered in practice in measurements of interest, we can replace $\sin\phi$ by ϕ in radians in almost all expressions.

The method of spin rotation angle measurement outlined above is also employed in neutron spin echo spectroscopy.[25] However, those spectrometers are designed to measure not the forward scattering amplitude but the double differential cross section $\frac{d^2\sigma}{d\Omega dE}$, which is directly proportional to the dynamic structure factor of the target medium $S(Q,\omega)$ which can reveal information on the structure and dynamics of condensed media.[26–28] This is done by manipulating the quantum mechanical state of the neutrons between the polarizer and the polarization analyzer using magnetic fields so that the neutron enters the sample region in an entangled state involving the neutron helicity states and the neutron energies and momenta. Clear quantum mechanical descriptions of the operation of various types of neutron spin echo spectrometers can be found in the literature.[29]

B. Physical origin of f_{PV}

Any interaction which generates a $\vec{\sigma}_n \cdot \vec{k}_n$ term in the neutron forward scattering amplitude will give rise to a corresponding neutron rotary power. As a simple example to show how the neutron rotary power depends on key features of this interaction, consider a vector boson X_μ coupling to a fermion ψ with an interaction of the form $\mathcal{L}_I = \bar{\psi}(g_V\gamma^\mu + g_A\gamma^\mu\gamma_5)\psi X_\mu$, where g_V and g_A are the vector and axial couplings. Z boson exchange in the Standard Model is a particular example of such an interaction. In the nonrelativistic limit, $\mathcal{L}_I$

gives rise to the potential

$$V(r) = \frac{g_V g_A}{2\pi} \frac{\exp(-r/\lambda)}{r} \vec{\sigma} \cdot \vec{v}, \tag{21}$$

where $\lambda = 1/m_X$ is the interaction range, m_X is the mass of the vector boson, $\vec{s} = \vec{\sigma}/2$ is the spin of the polarized particle, and r is the distance between the two interacting particles. Using the Born approximation, one can calculate the relation between f_{PV} and the parameters of the potential, and the spin rotation angle per unit length can be expressed directly in terms of the vector and axial vector couplings, the range of the interaction, and the number density of scatterers in the medium,

$$\frac{d\phi_{PV}}{dL} = 4 g_V g_A \rho \lambda^2. \tag{22}$$

This expression should make it clear that the length scale of the interactions that can be probed by a forward scattering observable such as the neutron rotary power has nothing to do with the energy or momenta of the projectile and depends instead on the form of the parity-odd interaction. For spin-independent interactions, this conclusion follows directly from the optical theorem, which relates the imaginary part of the forward scattering amplitude to the total cross section, and it is also true for the real part of the forward scattering amplitude involved in neutron spin rotation.

III. EXPERIMENTAL METHOD

The spin rotation apparatus shown in Fig. 1 must distinguish small PV rotations from rotations that arise from magnetic fields. Magnetic fields are minimized by surrounding the target with a magnetic shield. ϕ_{PV} is isolated by alternately moving the medium in front of and behind a neutron spin precession coil and measuring the change in the spin rotation angle. Figure 2 shows the arrangement of the various magnetic fields and polarization components of interest. Neutrons polarized along $\hat{y}$ enter a central precession coil with an internal magnetic field along $\hat{y}$ (π-coil) which precesses a spin component along $+\hat{x}$ to $-\hat{x}$. The contribution to the total rotation angle coming from parity violation in the medium therefore changes sign as the medium is moved from a position in front of the π-coil to a position behind the π-coil. To further suppress systematic uncertainties and noise, the beam and apparatus are split into right and left halves, and the targets are filled so that the medium occupies the chamber downstream of the π-coil on one side and the chamber upstream of the π-coil on the other side. The PV components of the neutron spin rotation angle have opposite signs on each side, and the difference of the two rotation angles is insensitive to both static residual magnetic fields and any common-mode time-dependent magnetic field integrals along the neutron trajectories. If the motion of the medium in front of and behind the π-coil does not change the spin rotation angles experienced by the polarized neutrons as they pass through the residual fields in the target chamber or the phase space of the transmitted neutrons entering the neutron polarization analyzer, the difference in the total rotation angle upon motion of the medium isolates the parity-odd neutron spin rotation from the target. The measurement is also conducted with the current in the π-coil reversed to cancel any systematics coming from stray fields from the coil outside the precession region. Data are also taken with the current in the π-coil set to zero so that the spin rotation from the medium is not reversed. In this case, the difference between the total spin rotation angle for the two target states must be zero in the absence of systematic effects.

Possible systematic uncertainties can arise from various types of deviations from the idealized conditions described above. We will describe some of these systematic effects later in a general way but their size depends in detail upon the neutron scattering properties of the target medium and a detailed description of systematic uncertainties must be conducted on a case-by-case basis for each particular medium.

The neutron polarimeter employs a neutron polarization analyzer to measure the $\hat{x}$ polarization component of a neutron beam initially polarized along the $\hat{y}$-axis and traveling in the $\hat{z}$-direction. To understand the polarimeter operation, consider the behavior of the neutron polarization direction, which emerges along the $\hat{y}$-direction from the neutron polarizer and is adiabatically guided into a near-zero field region. In the absence of magnetic fields and parity violation in the target region, the neutron polarization direction is unchanged as it

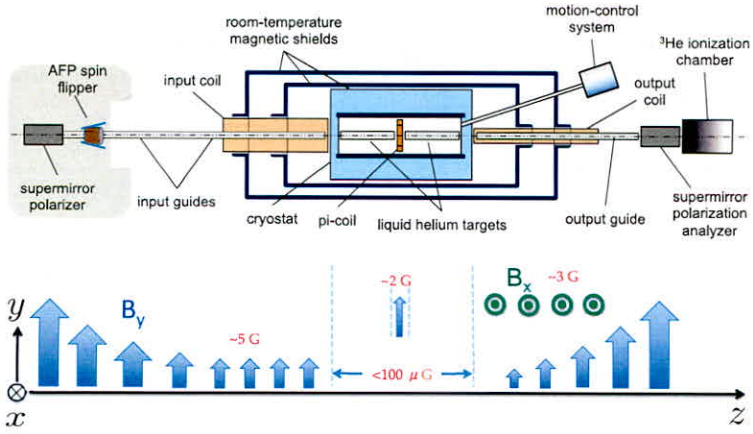

FIG. 1. Overview of an apparatus to measure parity-odd neutron rotary power. The typical values for different components of the magnetic field (including the magnetic field inside the π-coil in the midst of an otherwise near-zero field region) are plotted below the diagram.

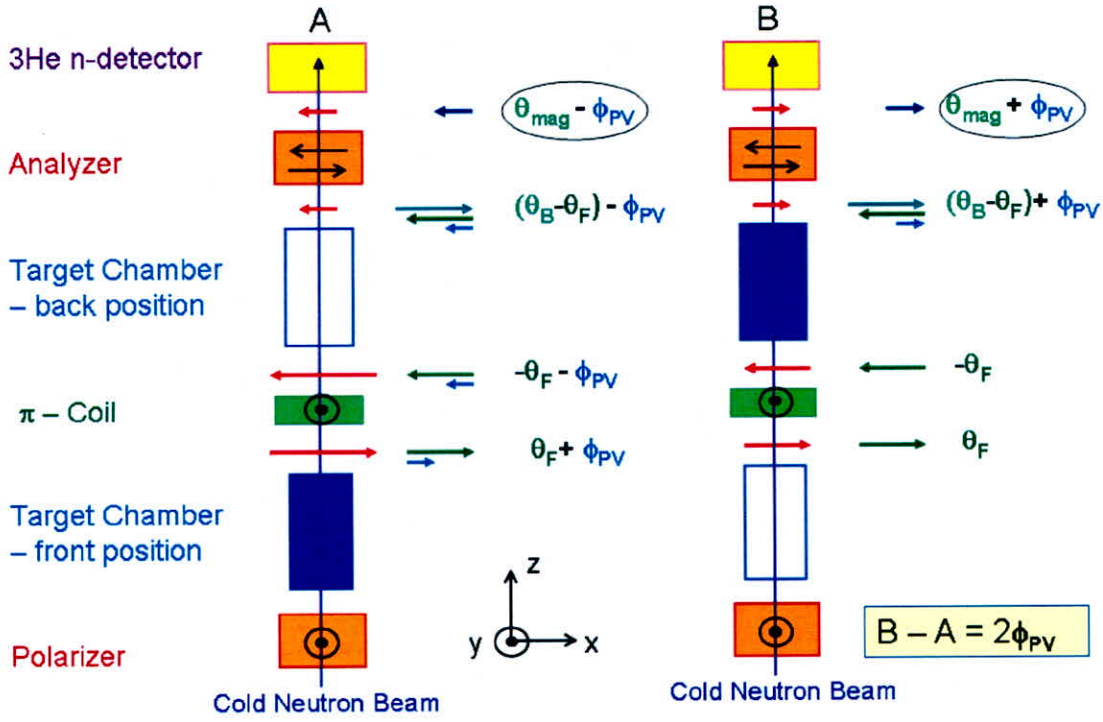

FIG. 2. Conceptual diagram (top view) illustrating the strategy to isolate the PV neutron spin rotation signal in the presence of a large background from residual longitudinal-magnetic-fields. The arrows show the projection of the neutron polarization-vector onto the plane of the figure at different points along the apparatus and for two different target states A and B, which correspond to the liquid present in the upstream and downstream chamber, respectively.

emerges from the zero field region. As discussed in Sec. I, one can in principle measure the spin rotation angle by rotating the axis of the polarization analyzer by $\pm\frac{\pi}{2}$ and measuring the difference between the transmitted intensities. Because this is mechanically impractical, instead one rotates the neutron spins adiabatically by $\pm\frac{\pi}{2}$ between the target exit and the analyzer using adiabatic spin transport in magnetic fields. This adiabatic spin transport is effected by a static magnetic field created by magnetic field coils orthogonal to the beam and desired spin analysis directions (see Fig. 1). The coil winding densities vary appropriately along the neutron beam direction in such a way that the total magnetic field changes direction by $\pm\frac{\pi}{2}$. Neutrons exit this field region non-adiabatically by passing through a current sheet at the end of the target region. (A similar current sheet at the beginning of the target region provides a transition from the polarizer guide field into the low-field region). The fields are arranged to change slowly enough in space that the projection of the neutron polarization vector on the magnetic field direction upon the entrance of the polarized slow neutrons into the field is an adiabatic invariant. The asymmetry in the count rates for an imperfect polarizer and polarization analyzer is given by

$$\frac{N_+ - N_-}{N_+ + N_-} = PA\sin\phi, \tag{23}$$

where P is the neutron polarization from the polarizer, A is the analyzing power of the analyzer, and ϕ is the neutron spin rotation angle. The product PA can be easily measured by applying an external magnetic field to set ϕ to a known angle, either with an internal magnetic field or a mechanical reorientation of the directions of the polarizer or analyzer.

The neutron polarimeter employs three types of oscillations at different frequencies to isolate the parity-odd component of neutron spin rotation from the medium. Here, we list typical values we used in our liquid helium measurement. The $\pm\frac{\pi}{2}$ oscillation of the helicity of the magnetic field of the output coil operates at the highest frequency (1 Hz). The reversal of the current in the π coil cancels any rotations caused by its stray fields, and the measurement with the π-coil current set to zero measures any systematic effects correlated with the medium motion and occurs at a lower frequency than the transport field helicity reversal (5×10^{-2} Hz). The motion of the medium to positions in front of and behind the π-coil which isolates the parity-odd component of this total rotation angle is conducted at the lowest frequency (about 7×10^{-4} Hz). As the latter frequencies fall into a regime where the dynamics is susceptible to $1/f$ noise, higher frequencies are desirable and could be practical for other target media. The frequency of target motion is relatively slow, so we also choose to analyze the time series of spin rotation angles using algorithms which suppress possible effects from slow external magnetic field variations which can leak into the target region.[30]

A. Apparatus design considerations

Since the parity-odd neutron spin rotation angle is proportional to the target length, there is an advantage in choosing this length to be as long as possible. In practice, an optimum target length exists as there is a trade-off between the increase in the rotation angle with target length and the decrease in the statistical accuracy due to the increased fraction of neutrons scattered out of the forward direction. To estimate the

uncertainty in $\sin\phi$, we start with the equation above and sum the uncertainties in quadrature for uncorrelated measurements N_+, N_- and polarization product, PA. In terms of the total count-rate of $N_{tot} = N_+ + N_-$, where $N_+ \approx N_- \approx \frac{1}{2}N_{tot}$, the uncertainty $\sigma_{\sin\phi}$ in ϕ in terms of the total counts and the uncertainty σ_{PA} in PA is

$$\sigma_{\sin\phi} = \frac{1}{PA}\sqrt{\left[\frac{1}{N_{tot}} + \sin^2\phi(\sigma_{PA})^2\right]}. \quad (24)$$

We can optimize the signal/noise ratio by considering how both depend on the target thickness. The parity-odd spin rotation angle $\phi_{PV} \propto \rho x$ is proportional to the target density ρ and the target length x. The statistical uncertainty is $\sqrt{N} = \sqrt{N_0 e^{-\rho\sigma x}}$, where σ is the total neutron cross section. Maximizing the ratio of signal to statistical uncertainty gives an optimum target thickness of $x = 2/\rho\sigma$, which sets the scale for the target length. Since the total neutron cross section for materials is typically a strong function of energy in the slow neutron regime, the optimum target length will depend in practice on the details of the neutron spectrum and the internal structure of the target medium.

The neutrons pass through the target and a neutron polarization analyzer and are detected in a segmented ^{3}He ionization chamber operated in current mode.[31] Since the uncertainty of a measurement in current mode can be greater than the lower bound set by the $\sqrt{N}$ neutron counting statistics assumed in the noise derivation above,[32] one must take care that no additional noise sources limit the statistical accuracy of the angle measurement. The most serious source of extra noise above $\sqrt{N}$ neutron counting statistics in this measurement comes from nonstatistical fluctuations in the reactor neutron source intensity in the 1 Hz frequency band set by the frequency of reversal of the output coil current used to measure the rotation angle. To further suppress systematic uncertainties and possible noise associated with fluctuations in the neutron source intensity, residual magnetic-fields, or target density, the beam, target chamber, polarimeter, and ion chamber are also split into separate but parallel right and left halves. The noise in the ratio of the current-mode signals in the ion chamber should therefore be dominated by neutron shot noise. The spatial pattern in which the target chambers are filled in the measurement is chosen so that the PV components of the spin rotation are always in opposite directions in each half of the beam. With this arrangement, the difference in the ratio of the ion chamber currents in the polarimeter upon moving the liquid in the chambers is proportional to the parity-odd spin-rotation-angle.

In addition to its task of measuring the spin rotation angle from the intensity differences through the polarization analyzer, the ion chamber is also used to measure possible systematic effects from magnetic fields. The ion chamber electrodes are segmented into four quadrants, one upper and one lower quadrant for each sub-beam. The ion chamber is also segmented longitudinally along the neutron beam to allow some neutron energy discrimination to be made. The parity-violating neutron spin rotation is independent of neutron energy for slow neutrons, whereas the spin rotation angle due to longitudinal magnetic fields is proportional to the time spent in the field and therefore the neutron velocity. Due to the $1/v$ dependence of the neutron absorption cross section in the ^{3}He-rich ion chamber, higher energy neutrons penetrate farther into the chamber on average. So, the currents collected at different segments along the beam sample different neutron velocity classes. A true parity-violating signal must give the same asymmetry on all segments. We exploit this feature of the ion chamber in combination with analysis of calibration data taken with the π-coil off to measure the systematic effects.

B. Experimental apparatus

The apparatus we describe here was operated with a liquid helium target at the NG-6 slow neutron beamline at the National Institute of Standards and Technology (NIST) Center for Neutron Research (NCNR). At the NCNR, neutrons from a 20 MW reactor were moderated by a cold source and transported 68 m north along an evacuated rectangular ^{58}Ni-coated guide to the NG-6 end station.[33] The neutrons were polarized vertically by a polarizing supermirror[34] and entered the magnetic shield/target region using a glass neutron guide and a magnetic field from an input coil to transport and preserve the neutron polarization.[35] The target vessel was mounted inside a magnetic shield that was centered in a nonmagnetic liquid helium cryostat supported in turn inside two more layers of magnetic shielding. The liquid was moved between the four separate target chambers using a centrifugal pump immersed in a 4 K liquid helium bath outside the target with flexible tubes pulled by strings to determine which pair of target chambers fill or drain.[19] Internal fluxgate magnetometers indicate a typical internal axial magnetic field of 100 nT. Ten equally spaced coils were arranged around the outside of the vac-canister and connected to individual current supplies to provide magnetic field compensation inside a layer of cryogenic magnetic shielding that lined the cold bore. After the target region, an output coil and another float glass neutron guide conducted the transmitted neutrons to the polarization analyzer. The output coil adiabatically rotated the x-component of the neutron polarization by $\pm\pi/2$ in the $x - y$ plane through modulation of the current direction in one of two orthogonal solenoids. The neutrons exited the output coil and guide and passed through the polarization analyzer and ion chamber. Figure 3 presents a diagram of the neutron beamline and path along the spin rotation apparatus. It shows the magnetic field configurations used to maintain the neutron polarization upstream of the target and to manipulate the neutron polarization direction downstream of the target.

The π-coil generated an internal magnetic field of about 600 μT that precessed the transverse component of neutron spin about the vertical $\hat{y}$-direction. The amount of spin precession depends on both the strength of the magnetic field and the neutron velocity. The π-coil current was chosen to rotate the mean wavelength (approximately 0.5 nm) of the neutron beam by π radians. The π-coil consisted of a pair of side-by-side, 40 mm square cross section, 160 mm tall solenoids. To minimize magnetic flux leakage, the current in the two rectangular coils flowed in opposite directions with a set of three curved solenoids providing magnetic flux return at the

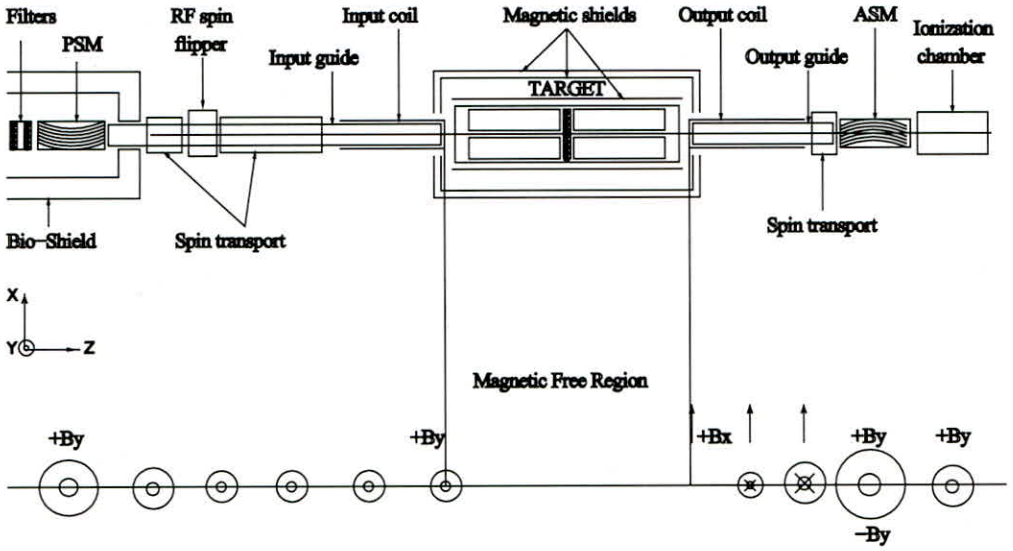

FIG. 3. Top view diagram of the spin rotation apparatus and the magnetic fields throughout the apparatus. A supermirror polarizer and an input coil prepared the neutron polarization and launched the polarized neutron into a magnetically shielded region containing the target. The target consisted of four chambers and a π-coil. After leaving the field free region, neutrons passed through a current sheet into a horizontal guide field which adiabatically rotated to the + or − vertical direction. The bottom sketch indicates the magnitude and direction of the magnetic field in each region of the apparatus. The dots show magnetic fields directed out of the page ($\hat{y}$); the cross means they point into the page ($-\hat{y}$).

ends. The leakage field was measured at less than 50 nT at a position of 1 cm from the center of the coil.

In describing the target, we will use the example of liquid helium. The measurement technique can be used for other media as well as long as sufficient care is given to avoid magnetic impurities and employ a nonmagnetic motion mechanism to move the target on either side of the π-coil. The liquid helium target consisted of a pair of vessels located upstream and downstream of the π-coil. Each vessel was partitioned into separate left and right-side chamber pairs, which created four identical target chambers that could each hold liquid helium. This partitioning effectively created upstream and downstream chamber pairs along the left and right-side sub-beams and formed two parallel experiments when combined with the polarimeter design. The target plumbing was designed so that whenever the upstream target chamber was filled, the corresponding downstream chamber emptied to a level below the neutron beam and vice versa. Alternately filling and draining diagonal pairs of target chambers with liquid helium created the two target states that were necessary to extract the parity-violating spin rotation angle ϕ.

In order to change target states, liquid helium needed to be non-magnetically moved between target chambers. Each target chamber possessed an inlet and a drain for moving liquid helium. Inlets from all four chambers were connected to a centrifugal pump immersed in a 13-liter liquid helium bath located in the bottom of a cylindrical vessel. The pump and drain system was operated outside of the target region by a motion-control system consisting of a stepper motor and driveshaft, which turned a centrifugal pump, and a pair of pneumatic linear actuators that were attached to the drains by strings. By operating the centrifugal pump, all four target chambers could be filled with liquid helium. Each drain was connected to a flexible drainpipe that could be moved above or below the height of the full or empty liquid helium levels inside the target chambers. By lowering a drain, a target chamber could be emptied of liquid helium and its contents returned to the bath.

Because of beam divergence or small angle scattering, some neutrons can reflect from a target chamber wall, be transmitted through the polarimeter, and counted in the ^{3}He ionization chamber. The critical angle for neutron reflection between helium and aluminum depends on the difference in the neutron index of refraction of the two materials, which is proportional to density and therefore changes with the liquid or gas state of the helium. These differences can cause systematic effects through target-dependent neutron beam intensity and phase space changes coupled to residual magnetic fields in the target region. This subclass of neutron trajectories was prevented from reaching the ^{3}He ionization chamber by collimation of the beam. Within each target chamber, a set of three ^{6}LiF-plastic collimators prevented neutrons from reflecting off the chamber walls and reaching the detector.

1. Data acquisition

The role of the data acquisition system was twofold. It controlled sequencing the polarimeter through its various states and it counted the number of neutrons detected in each state.

A 2.5 GHz Intel P4 personal computer with 512 MB RAM ran the Microsoft WindowsXP Professional operating system. The acquisition code NSAC (for Neutron Spin Acquisition and Control) was developed using a combination of Microsoft's Visual C++ 6.0 and National Instruments' Lab WindowsCVI. This environment provided the interface to a National Instruments PCI-6031 card which read all data from the experiment including graphics displays. RS232 communication was used for slow control functions such as reading temperatures and cryogen levels and controlling cryogen

flows in the target. All input and output functions including user interaction and graphic displays were handled by Lab Windows. The remaining work flows and underlying architecture were written in C++. All data from the experiment were read by a National Instruments PCI-6031 card. Data read from the experiment included the ion chamber signals and the cryogenic liquid level and temperature sensors. Communications originated from the PCI-6031 and also from Universal Serial Bus (USB) to RS232 serial communication ports. These devices issued commands to the motor controller of the liquid ^{4}He pump and to the power supplies for the input and output coils and the π-coil.

Currents from each of the 16 ^{3}He ion chamber sectors were separately integrated for the time spent in each polarimeter state and gave a value proportional to the number of detected neutrons. The absolute calibration between integrated charge and the number of neutrons absorbed was not needed for the measurement of the neutron spin angles as they were calculated from the transmission asymmetry in terms of ratios. Figure 4 shows one channel of the integrator electronics. It used one half of a Burr Brown AFC 2101 dual switched integrator. The external capacitor $C1$ determined the voltage for a given amount of accumulated charge. Its value was 0.3 nF for the front 12 charge collection sectors and 0.1 nF for the back section as the neutron flux is reduced at the back end of the detector. Diodes PAD1 protected the inputs from voltage transients. The reset function was used to periodically discharge the capacitor after switching to a new configuration of the polarimeter. The select and hold functions were not used as the output of each integrator fed directly into an analog to digital convertor (ADC) channel on the data acquisition board. The linearity of the electronics was verified by insertion of appropriate test currents into the ion chamber electrodes.

Timing for NSAC is derived from on-board clocks in the PCI-6031. The board is configured to read all ADCs every 0.1 s. The acquisition thread runs at highest priority and polls the status of ADC conversions every millisecond. When all conversions are completed, a service routine copies data from the hardware and serves as the master timing event for sequencing the states of the polarimeter. At every tenth read, the polarimeter is advanced to its next state and the integrators are reset. A partial time line showing these events is given in Figure 5. The first line in the figure is a hardware output signal that is sent when ADCs finish converting. Like other non real-time systems, the Windows operating system has a variable and unpredictable latency when responding to events. The next line represents the time the event's service routine is running and shows this variable latency in the response.

The next line shows reset enable being set to high after the service routine completes. The effect of fluctuating reset timing on the integrator output is avoided using two external monostable multivibrators. The first is triggered by the ADC convert signal and shown as convert delay. When reset is enabled, the rising edge of convert delay triggers the second monostable multivibrator which then resets the integrator.

The difference between integrator outputs at ADC read 9 and previous read 0 (vertical dashed lines) gives the integrated charge for each channel in a 0.9 s time interval. The 16 bit ADCs have a range of ±10 V. Typical currents were in the range of 4–6 nC per channel. The noise added by the data acquisition system was ±1 pC. The last line shows timing for transitions between magnetic fields corresponding to the various polarimeter states. These states are described in the discussion surrounding Figure 6. The 0.1 s dead time window is sufficiently long that latency fluctuations do not affect the field values.

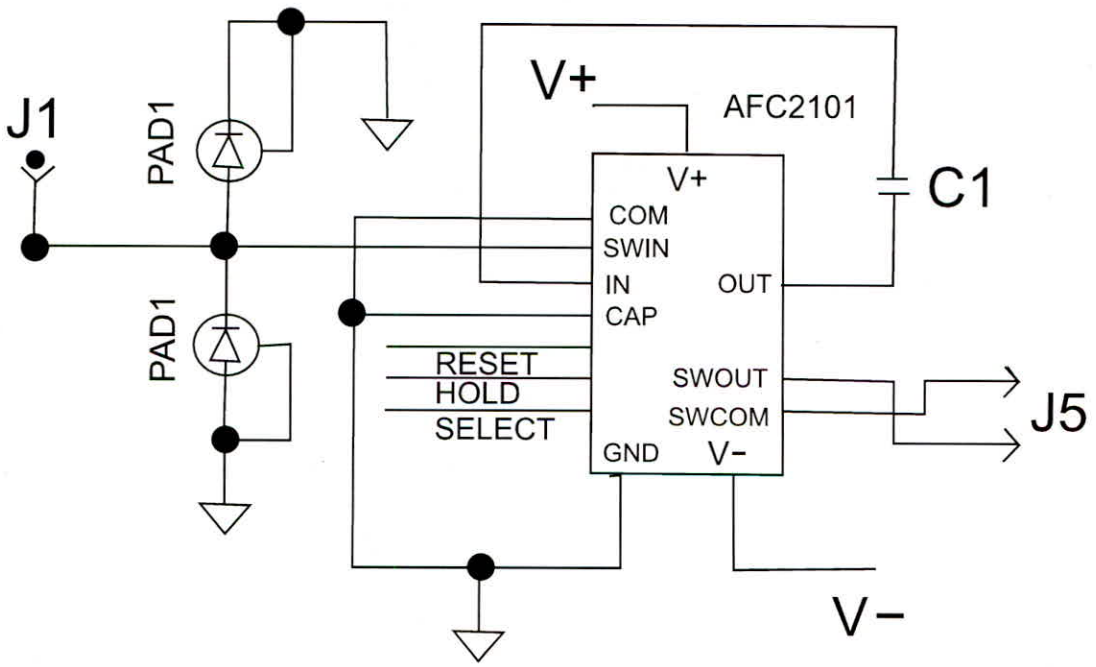

FIG. 4. The figure shows the schematic for one of 16 channels of current integration. It uses 1/2 of a Burr Brown AFC2101 dual switched integrator. All components except for the integration capacitor C1 and protection diodes PAD1 are included on the chip.

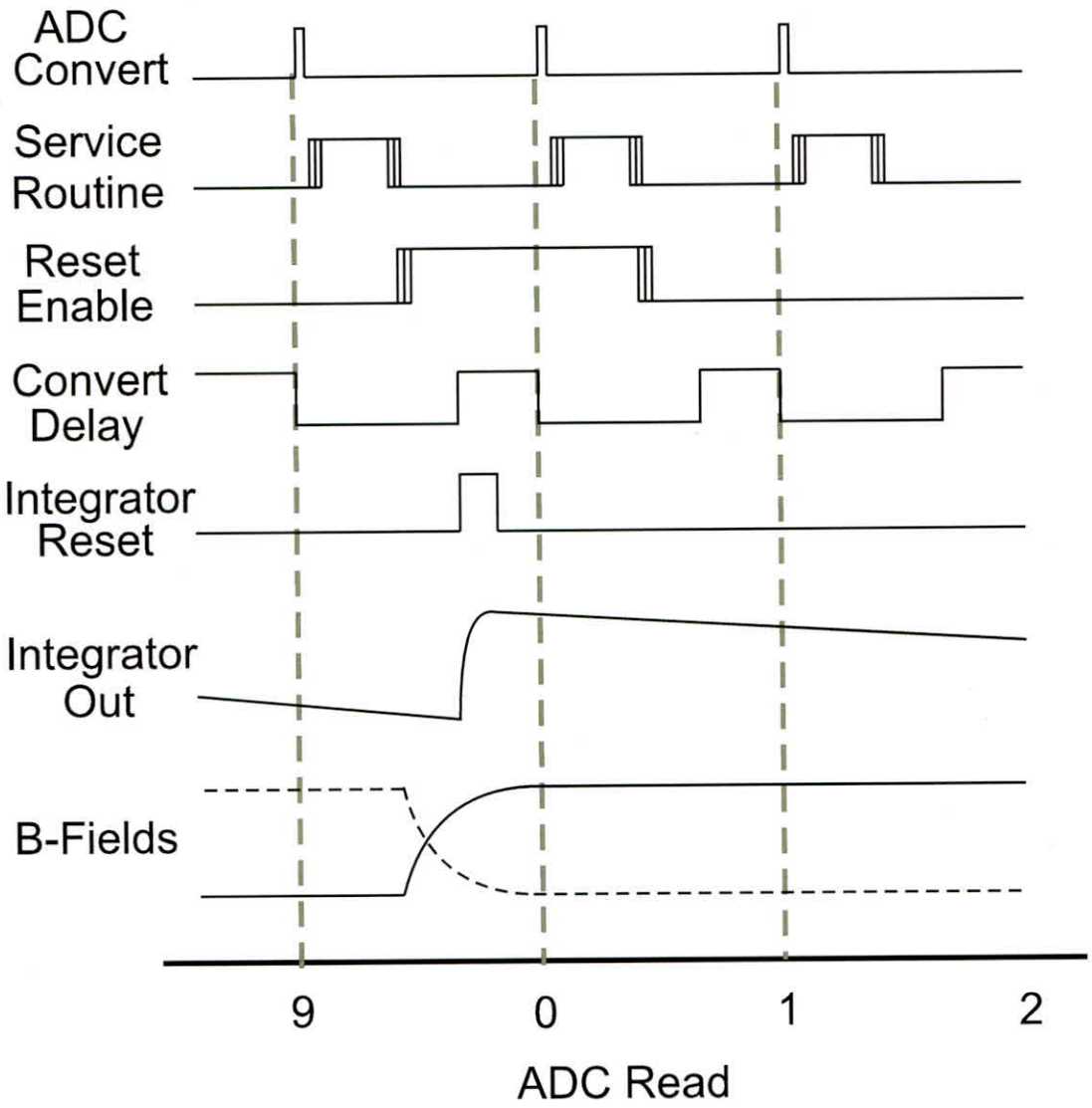

FIG. 5. The figure shows event timing in the data acquisition program. ADCs measuring integrated charges from ion chamber sectors are read out at 0.1 s intervals. After every tenth read (number 9 in the plot), current integrators are reset and magnetic field configurations are transitioned to new values. A data point consists of differences between the last and first ADC readings for each channel.

After a pre-programmed sequence of magnetic field values completes, a separate thread controls valves and the liquid He pump to change the target configuration. Cryogenic level and temperature sensors are also read and included in the data stream. A complete sequence consists of 10 angle measurements for each of three π-coil states, repeated 5 times for each target configuration.

IV. POLARIMETER CHARACTERIZATION

In this section, we describe how the operation of the neutron polarimeter was characterized and calibrated. This calibration work is divided into three fairly distinct activities: (A) simulation and measurement of neutron spin rotation angles generated by applied longitudinal magnetic fields, (B) measurement of the polarizer-analyzer product PA by applying rotations of the neutron spin orientation, and (C) calibration of the response of the ion chamber to a known spin rotation angle using its velocity sensitivity from longitudinal segmentation as described below using the polarized neutrons themselves as a magnetometer.

We calibrated the polarimeter using longitudinal magnetic fields applied inside the target region. Since the neutron spin rotation angles in this case depend on the time spent in the field and therefore on the velocity distribution of the neutron beam, this characterization also requires some knowledge of the neutron energy spectrum in the beam. We therefore developed a simulation of the polarimeter which included the key features of the transport of the neutron momenta and spins through the relevant neutron optical elements and magnetic fields. We constrained the simulation inputs using measurements of the beam properties at various points along the apparatus and used it to calculate the predicted neutron spin rotation angles for various magnetic field configurations.[38] The simulations and data are in agreement at the few percent level, which is within the accuracy with which the fields were determined.

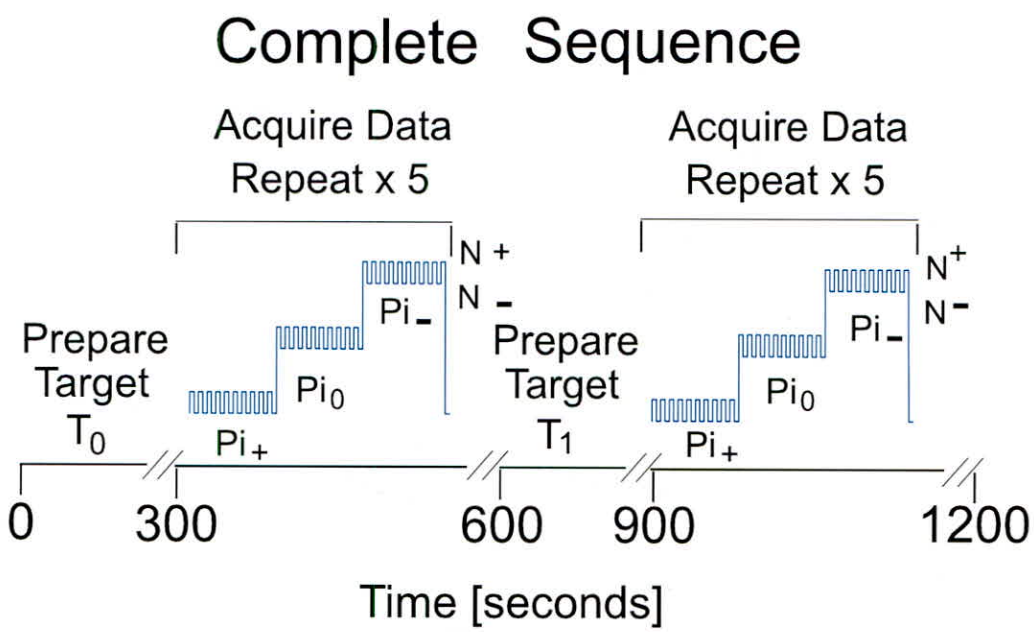

FIG. 6. The complete sequence of measurements shown is required for each determination of ϕ. N^+ and N^-, each with a duration of 1 s, are polarities of the output coil discussed in Sec. IV B. Pi_+ and Pi_- are polarities of the Pi-coil current when it is on and Pi_0 when it is off. The 2 target configurations are given by T_0 and T_1.

A. Polarimeter calibration with magnetic fields

The initially vertically polarized neutrons precess in a longitudinal magnetic field by an angle

$$\theta_m = \gamma_n B_L (L/v), \tag{25}$$

where γ_n is the neutron gyromagnetic ratio (183.25 (rad/s)/μT), and L and v are the neutron path length and velocity. The angle calibration therefore depends on knowledge of the neutron velocity spectrum in the target region and the longitudinal magnetic field integral along the neutron trajectories. The velocity spectrum can be measured directly in principle. As this was mechanically awkward for our liquid helium target and since our measurement was focused on search for a very small rotation angle, we chose to infer the velocity spectrum in the target region through measurements of the beam intensity and spectrum at various points in the apparatus before and after the target combined with a simulation. We compared calculations of the fraction of the beam absorbed in each of the four ion chamber detector segments at the end of the apparatus to data using

$$N_2(E_n) = N_1(E_n) e^{-\rho d \sigma(E_n)}, \tag{26}$$

where N_1 and N_2 are, respectively, the neutron counts before and after each segment with energy E_n. ρ is the number density of the ^{3}He gas, d is the depth of each segment, and $\sigma(E_n)$ is a fit to the energy dependent n-^{3}He absorption cross section data[36,37] which are $1/v$ to high accuracy.

The depths of the four detector segments were measured to be 2.8, 6.4, 7.4, and 8.7 cm from upstream to downstream. The ion chamber was filled with a partial pressure of 0.22 bar of ^{3}He. Figure 7 shows the simulated wavelength spectra after the 4 detector segments. Table I lists the simulated percentage of the absorbed neutrons in each detector segment in comparison with the data. The measurements are consistent within a few percent for each segment with a simulation described below.

The total spin rotation angle at the detector was also compared with data taken under amplified magnetic field conditions in the target. Since there are guide fields outside

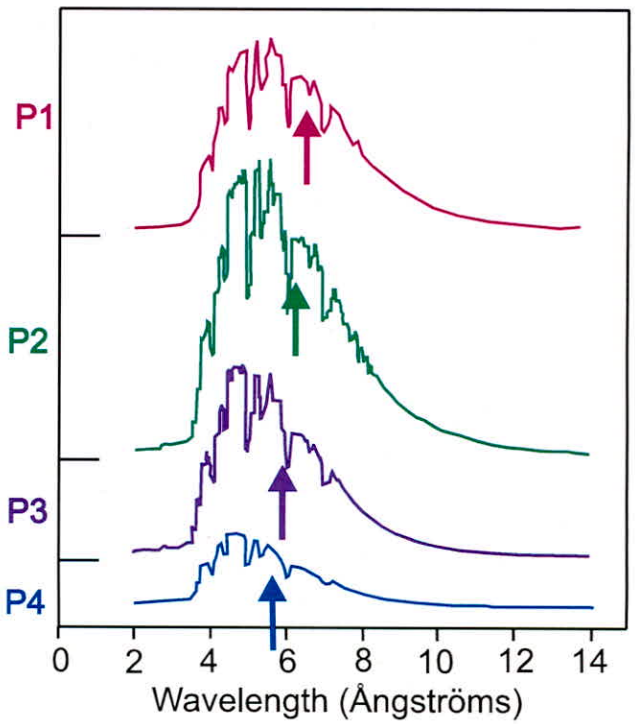

FIG. 7. Results of the simulation are shown giving the wavelength distributions of neutrons that stop in each of the 4 longitudinal sections of the ^{3}He ion chamber. Each section is sensitive to a different part of the neutron beam's energy spectrum as shown by arrows pointing to the means of each distribution. P1 refers to the entrance segment.

TABLE I. Fraction of the incident neutron beam absorbed in each detector segment.

Segment	1(%)	2(%)	3(%)	4(%)
Simulation	25	35	20	11
Measurement	25	37	21	7

the low-field target region, Eq. (25) was used in each apparatus component only within the target region with magnetic field values given by measurement. The simulated rotation angle of 116 mrad in the applied B-field gradient with the π coil off is higher than the measured rotation angle for data runs with this field condition of 98 mrad. The most likely source for the difference between the rotation angles from simulation and data comes from the stray magnetic fields between the target region and the entrance and exit of the input and output coils which are not well characterized. Although these fields were measured before data taking commenced, these fields can change upon demagnetization of the shields and we therefore do not expect to be able to achieve better agreement between simulation and measurement than in Table I.

B. Polarizer-analyzer product measurement

Recall that the total spin rotation angle through the apparatus is determined by measuring the neutron intensity transmitted through the polarization analyzer for the two helicity states N^+ and N^- of the output coil magnetic field. Ideally, the resulting asymmetry in the count rates given by Eq. (20) isolates the component of the rotated neutron spin in the plane normal to the neutron momentum. The PA product of the polarizing power of the polarizer and the analyzing power of the analyzer is related as usual to the measured asymmetries by Eqs. (27) or (28),

$$\mathcal{A}^0 = PA^0 \sin\phi, \tag{27}$$

$$\mathcal{A}^\pi = PA^\pi \sin\phi, \tag{28}$$

where we define PA^0 and PA^π as the polarizer-analyzer products for π-coil off and on states, respectively. Unfortunately, there are some small corrections which must be applied to these PA products so that they properly isolate the parity-odd rotation of interest in the presence of nonzero background magnetic fields in the target region in a neutron beam with a velocity spread. If the neutron beam was monoenergetic with the π-coil internal magnetic field tuned to precess all the neutron spins by π radians and if there were no residual magnetic fields in the target region, then $PA^0 = PA^\pi$. We choose to use a broad spectrum of neutron energies to improve the statistical accuracy of the angle measurement. In this case, however, the PA product in the apparatus is different depending on the state of the π-coil. The largest source of this difference comes from the distribution of neutron velocities in the beam, which means that magnetic field in the π-coil only precesses neutron spins of some average velocity by π radians, thereby over-rotating the slower neutrons and under-rotating the faster neutrons and reducing the size of the projection of the rotated polarization components onto the polarization analyzer.

These polarization products for the apparatus are measured by mechanically tilting the input coil (and therefore the polarization direction of the neutrons entering the magnetically shielded region) by a few degrees about the beam axis and measuring the corresponding asymmetries. PA products are measured for each of the 16 elements in the ion chamber. Differences in the PA products for the different ion chamber collection plates can come from nonuniformities in the polarization analyzer as a function of neutron energy and spatial location on the analyzer, spin transport efficiency, etc. The differences in the PA product with the π-coil on and off, however, come only from the dominant effect from the spread in neutron velocities. It is therefore convenient to define $d = -PA^\pi/PA^0$ which measures the reduction in PA from the neutron velocity spread. Furthermore, the average polarization products PA_W and PA_E for the west and east sides of the apparatus are required for subsequent data analysis since the parity-odd signal is obtained from differences in west and east side angle measurements. We express the difference between the east and west polarization products with a multiplicative factor $\omega^{0,\pi}$ for the west side products $PA_W^{0,\pi}$,

$$\omega^{0,\pi} = \sqrt{PA_W^{0,\pi}/PA_E^{0,\pi}}. \tag{29}$$

By symmetry, east side factors are given by inverse values, $1/\omega^{0,\pi}$. East-west spin angle differences would then be obtained from the corrected PA products,

$$\mathcal{A}_W - \mathcal{A}_E \Longrightarrow \frac{1}{\omega}\mathcal{A}_W - \omega\mathcal{A}_E. \tag{30}$$

PA product measurements were made periodically throughout the experiment. Results for PA^0 and d averaged over the east and west sides of the beam are shown in the upper plot of Fig. 8, where statistical uncertainties in all plots are the sizes of the plot symbols. The scatter in these measurements was greater then their individual uncertainties due to changes in the residual magnetic fields after demagnetization of the mu-metal magnetic shields. After each demagnetization, the shielding factor and coil geometry do not change significantly, and therefore, for purposes of data analysis, the PA products are assumed to stay constant for all runs conducted between the measurements. The shaded bands give average uncertainties per point determined from uncertainties in the means. The lower plot of Fig. 8 gives the east-west difference of the polarization product for each measurement expressed in terms of the factor $\omega^{0,\pi}$ defined above. The squares (red online) correspond to ω^π and the triangles (blue) to ω^0. The fractional east-west deviations are as large as 2%.

C. Calibrating the polarized neutron magnetometer

To use the ion chamber as a magnetometer, we need to know the neutron velocity spectrum as it passes through the apparatus and enters the ion chamber. The slow neutron energy spectrum of the beam used in the experiment has an approximately Maxwellian spectral distribution with absorption dips from upstream materials which diffract certain neutron energies out of the beam. This distribution can be measured directly, and in our case, it was sufficient to use the expected

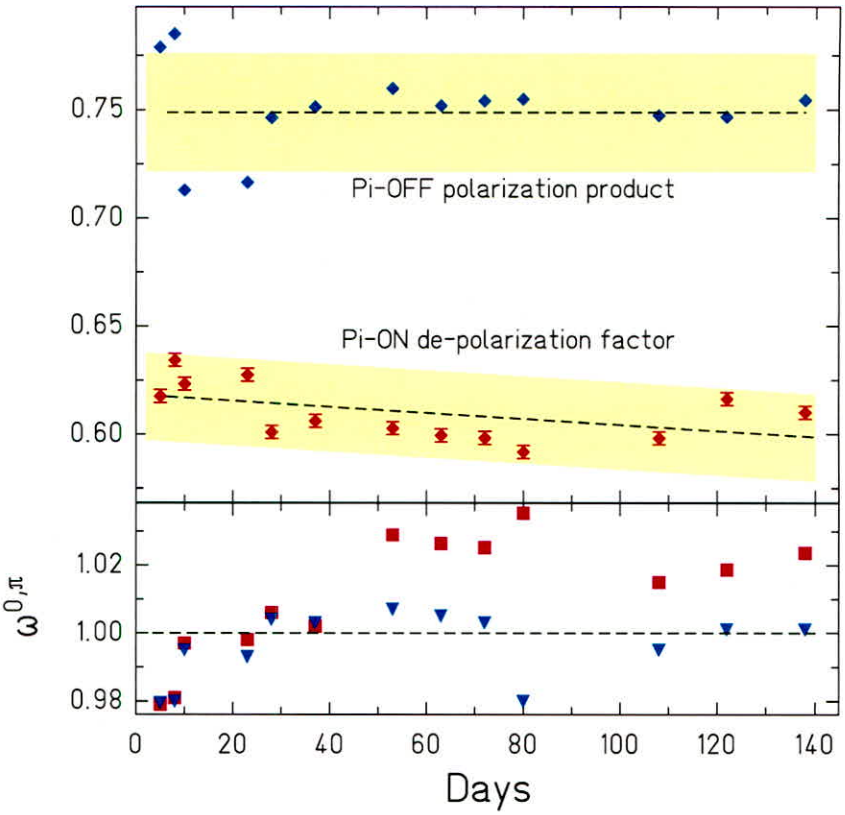

FIG. 8. The upper plot shows the average of the west and east polarimeter polarization products PA with the π-coil off and corresponding d factors when it was on. The lower plot gives ω^0 (triangles) and ω^π (squares), the fraction by which each side differs from the average. Shaded bands show average uncertainties per point based on their means.

spectrum from simulation. Figure 7 shows results from our Monte Carlo simulation which takes the spectrum measured from the exit of the neutron guide and propagates it through the apparatus to the ion chamber's 4 longitudinally segmented sections. Sections are labeled P1 through P4 where P1 is at the entrance of the detector. Mean wavelengths for each section are shown in the plot by vertical arrows. Integrals of these distributions give the relative number of neutron capture reactions and therefore the relative signals sizes in each section. The measurements of the fractions of the neutron beam absorbed in the 4 longitudinal sections of the ion chamber were in good agreement with measured data as discussed in Sec. III A. The spectrum hardens as the neutrons penetrate further into the chamber due to the $1/v$ dependence of the neutron absorption cross section on ^{3}He. The measured spin rotation angle per longitudinal ion chamber section allows the component of the spin rotation from the internal magnetic fields in the target, which depends on the time that the neutron spends in the field, to be separated from the parity-odd component from weak interactions, which is independent of the neutron energy in this regime.

Given the relation between the neutron energy and its probability to be detected in one of the longitudinal sections, θ_m in Eq. (25) can also be written in terms of the change in spin rotation angle per plane divided by the fractional change in the mean neutron de Broglie wavelength per plane. Rewriting Eq. (25) where the mean wavelength varies with plane position, P, we have

$$\theta_m = \frac{m_n \gamma_n B_L L \lambda}{\hbar}, \tag{31}$$

$$\theta_m = \left(\frac{1}{\lambda}\frac{d\lambda}{dP}\right)^{-1}\frac{d\theta_m}{dP}. \tag{32}$$

The first factor in the latter equation, namely, the fractional change in the average wavelength with respect to longitudinal location in the ion chamber, was calibrated experimentally using the measurements of spin angles from applied internal longitudinal magnetic fields. For these measurements, the target medium was removed and a current was applied to the trim coils surrounding the target region to produce a uniform 0.5 μT magnetic field. Figure 9 shows angles θ_m as defined above plotted for each ion chamber plane for the π-coil on and off, with statistical uncertainties smaller than the plotting symbols. The fractional change in θ_m per plane is obtained by dividing the linear fit to the π-coil off data in Fig. 9 by the average θ_m value gives $(1/\lambda)\frac{d\lambda}{dP} = (-6.96 \pm 0.09) \times 10^{-2}$.

This measured value is consistent with the measurements described above for systematic effects using internal fields of ± 0.5 and ± 1.0 μT and with the value calculated by a Monte Carlo simulation. As neutrons pass through the apparatus, their spectrum is shifted towards longer wavelengths from the energy dependence of neutron scattering from materials in the beam, so we expect and observe that the simulation using the energy spectrum as measured upstream of the target gives a smaller slope than the measurement using neutrons. By scaling

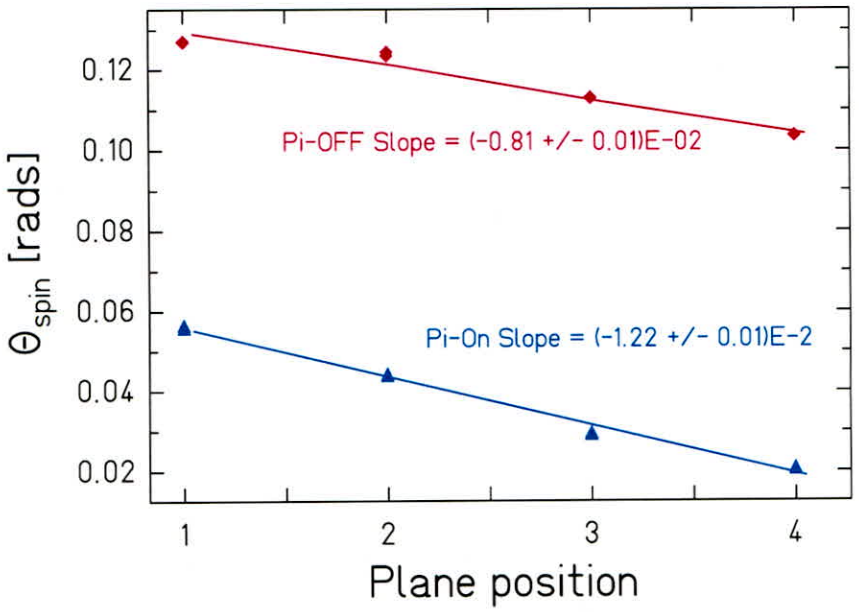

FIG. 9. Larmour precession angles measured by each longitudinal section of the ion chamber are shown for both π-coil on and off data for a $B = 5$ mG field. The sections correspond to plane positions 1 through 4 where neutrons enter the detector at position 1. The curves are linear fits to the data.

the value of θ_m determined in Fig. 9 by the spin rotation in a known longitudinal field, we determine the average longitudinal field in the target region between the input and output coils during production runs.

V. SOURCES OF STATISTICAL UNCERTAINTY

One can organize anticipated sources of uncertainty in spin rotation measurement into three classes: (a) multiplicative effects, which affect the scale of a true nonzero PV signal, (b) effects which increase the noise in the measurement significantly beyond the statistical limit given by $\sqrt{N}$ counting statistics, and (c) systematic effects which produce a nonzero signal in the experiment which is not due to PV spin rotation. The measurement requirements needed to address the first two classes of effects are relatively straightforward and are discussed in this section. A discussion of possible systematic effects (class (c)) is in general medium-dependent and a detailed treatment is beyond the scope of this paper.

The measurement of the product PA of the neutron polarization and the analyzing power of the neutron polarization analyzer makes the main contribution to uncertainties of class (a). The PA product is stable to high accuracy for a static apparatus. However, in practice, it must be measured periodically throughout the experiment as shown in Figure 8. The jumps in the PA values are understandable once it is realized that the demagnetization of the magnetic shield and the mechanical rotation of the input coil performed in measuring the PA product are not perfectly reproducible. In addition, unequal PA products for the two sides of the polarimeter reduce the cancellation of common mode rotations from magnetic fields as discussed earlier and can lead to more serious systematic uncertainties described in Sec. III B.

The largest effect in class (b) comes from fluctuations in the neutron intensity transmitted through the polarization analyzer and into the ion chamber. Recall that the frequency band relevant for our spin rotation experiment in liquid helium was around 1 Hz, which is the frequency with which the neutron spin rotation angle is measured by alternating the helicity of the magnetic field in the adiabatic neutron spin transport system described in Sec. II B. The choice of this frequency is determined in part by the speed with which the currents in the coils in the spin transport system of the polarization analyzer can be reversed and stabilized (at the upper end) and in part by the expected frequency dependence of the neutron beam intensity noise from the reactor (at the lower end). The $1/f$ noise in the reactor power combined with previous measurements leads us to expect that the beam intensity noise in a 1 Hz frequency band could be about five to ten times that from the $\sqrt{N}$ noise from the integrated number of neutrons in the same band. These expectations were confirmed by our measurements. Figure 10 shows the statistical distributions of the measured spin rotation angles in a liquid helium target for differences and averages of the polarimeter's west and east sides. The noise in the angle measurements is reduced through the removal of the common-mode reactor noise in the east and west halves of the neutron beam by a factor of 9. Clearly, the suppression of this extra noise from the source is an essential aspect of the polarimeter design.

To keep the contribution of this noise source below 1/10 of that from neutron counting statistics, we require that the two parallel sub-beams possess the same noise to 1% accuracy. Since the phase space of both halves of the beam is filled from the same neutron source as viewed by a long uniform neutron guide, we expect that the common-mode intensity fluctuations of the different halves of the beam will possess very similar power spectra, and since the two sub-beams are adjacent in space and are symmetrically located within several layers of magnetic shielding inside a nonmagnetic target system, we also expect the common mode noise in the spin rotations from

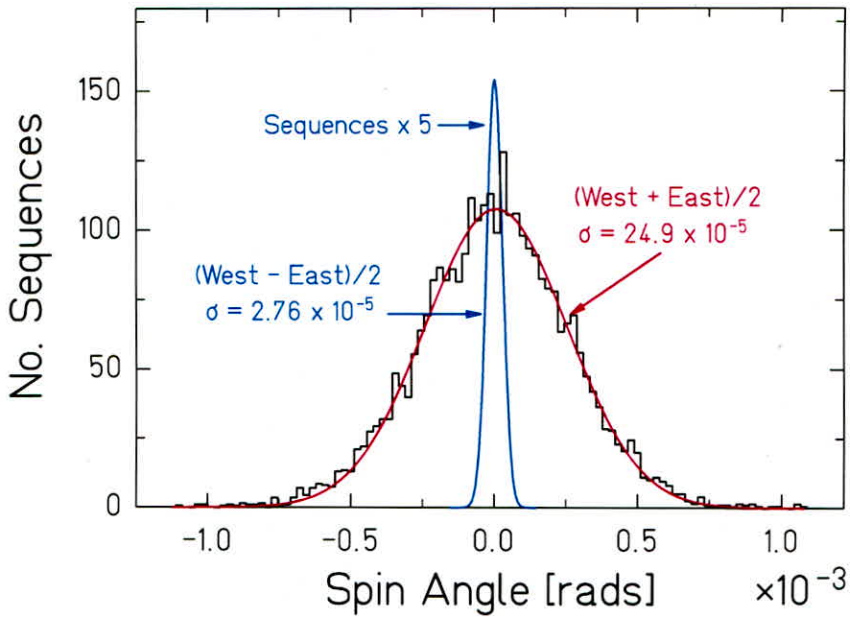

FIG. 10. Histograms of the total spin angles are shown with and without removal of the common-mode noise from reactor intensity fluctuations. Data from all three reactor cycles are included in these histograms. Note the ×5 scale change for the difference histogram.

fluctuations in the magnetic field also possesses similar power spectra.

Other effects which reduce the statistical accuracy come from noise in the intensity and/or beam spectrum from the reactor, from transmission through possible density fluctuations in the liquid target, from fluctuations of the neutron spin rotation angle analyzed by the polarimeter due to magnetic field fluctuations in the target region, from nonlinearities in the ion chamber response, and from extra noise in the ion chamber due to the current-mode measurement technique. We need the density of the targets to be stable at the 1% level in the frequency band of interest near 1 Hz for target density fluctuations to be negligible. Since bubbles in a liquid moving through the neutron beam can produce such density variations, this constraint requires, in practice, the need to suppress bubble formation. This can be done by (a) minimizing the heat load into the liquid vessel, (b) shielding the neutron beam from the internal surfaces of the target vessel where bubbles are most likely to nucleate and collect, and (c) operating the liquid in a slightly "superheated" state by maintaining a vapor pressure that is greater than the equilibrium vapor pressure of the liquid. The latter condition can be established in steady state in a cryogenic liquid target through careful design by taking into account the finite thermal conductivity of key target components. We saw no evidence for extra noise in the data which could be attributed to bubbles in the target.

The resulting noise in ϕ after removal of the common-mode noise can be compared to expectations based on neutron shot noise and the other noise sources. The neutron rate entering the ion chamber during normal running was $\Phi = 3.7 \times 10^7$/s. We estimate a 7% uncertainty in this value from the quadrature sum of the statistical uncertainty in the absolute flux measurement conducted on a portion of the beam plus its extrapolation to the full beam using relative beam intensity images (5%) and the absolute uncertainty (5%). We also must consider the extra noise due to the ion chamber and magnetic field fluctuations, which adds noise to the neutron spin rotation angle and therefore noise in the fraction of neutrons which reach the ion chamber. The ion chamber current-mode operation adds extra noise due to 3 effects: (1) fluctuations in the fraction of the neutron beam absorbed by the ion chamber, (2) fluctuations in the number of ions produced by the neutron absorption reaction in the chamber, and (3) current noise from the analog electronics. The ion chamber is calculated to absorb 97% of the incoming neutron fluence given the gas composition and pressure leading to a 1.7% noise increase. The number of ion pairs created per neutron absorbed in the ion chamber is about 2×10^4, leading to an extra 0.7% noise in the ion chamber current. The noise from the analog electronics is measured to be at the 0.1% level and is negligible in comparison. The linearity of the analog electronics of the ion chamber was measured using calibrated current sources to be better than 0.1%. An upper bound on the gamma sensitivity of the ion chamber was measured by blocking the slow neutron beam just in front of the ion chamber using a thick ^{10}B absorber which converts essentially all the neutrons in the beam into 0.5 MeV gammas: there was no observable signal above the electronic noise. We therefore neglect ion chamber nonlinearities or gamma sensitivity as possible sources of extra noise. Combining these uncertainties in quadrature gives an increase in the ion chamber noise above $\sqrt{N}$ of 1.8%. In our helium measurement, we observed that about 8% of the noise in the measured spin rotation angles comes from unfiltered magnetic field fluctuations. After removing this fraction of the noise, we obtained spin rotation angle noise from neutron counting statistics of 1.09×10^{-6}, 1.12×10^{-6}, and 1.18×10^{-6} in three different data sets which are in reasonable agreement with the

noise expected from $\sqrt{N}$ counting statistics of $(1.02 \pm 0.07) \times 10^{-6}$.

VI. POTENTIAL SOURCES OF SYSTEMATIC UNCERTAINTY

Here, we discuss the sources of potential systematic uncertainties in the neutron spin rotation measurement technique in a general way along with the strategies to suppress them. To establish that the systematic uncertainties in the measurement are much smaller than the statistical uncertainty, one can employ three independent methods to bound them. First, we either calculate or estimate potential individual contributions to the systematic uncertainty from all of the known physical effects in the target and apparatus which can generate a nonzero asymmetry in the absence of parity violation. This part of the analysis is essential input into the apparatus design and operation and can be used to place an upper bound on the expected systematic uncertainty, but carries the disadvantage that the relative weighting of some of these effects in the measured rotary power is difficult to determine. Second, one can conduct auxiliary measurements using the actual experimental apparatus which artificially amplify the size of possible systematic effects by a known factor and use our knowledge of how these effects scale for the conditions of the measurement to place an experimental upper bound on the systematics. This approach is quite effective in our case since almost all of the expected systematic uncertainties come from the internal magnetic fields in the target region. In previous work, we have already placed an experimental bound on the dominant set of systematic uncertainties which are independent of the magnetic field. Finally, as discussed in Sec. II and Fig. 6, one can measure the systematic uncertainty during data taking by interleaving measurement sequences with the π-coil turned off. In this section, we concentrate on the first two of these three methods to demonstrate the capability to achieve systematic uncertainties at the 1×10^{-7} rad/m level as this analysis can be presented in a fairly general way. We describe the general procedure for the use of the π-coil off data to bound the systematic uncertainty from the data but we plan to present the specific analysis in liquid helium in a subsequent paper.

By far, the most serious systematic effects in PV spin rotation experiments with cold neutrons are associated, directly or indirectly, with residual longitudinal magnetic fields. As an example, a 10 nT longitudinal field gives a spin rotation angle of about 2 mrad in 1 m for a neutron of wavelength 0.5 nm. In this case, if there is a systematic fractional difference in the magnetic field-induced rotations between the two target positions of 10^{-4}, then this effect is of the same size as our signal. Since our goal is to suppress all systematic effects to a size that is 1/10 of the statistical accuracy of the measurement, we must ensure that the amount of magnetic spin rotation is the same upon moving the target to $\approx 10^{-5}$ accuracy.

In the rest of this section, we assume an internal magnetic field of 10 nT in our quantitative estimates of systematic effects as we know from direct experience that this value can be achieved over the required volumes even with the target, π-coil, and other central components of the apparatus inside the inner magnetic shield. One can imagine ways to further suppress the internal magnetic fields if needed. We use liquid helium as an example and also comment on how the estimates are likely to change for other materials.

A. Sources of systematic uncertainty from neutron interactions in the target

It is useful to divide systematic uncertainties into two broad classes: those which depend on the scattering properties of the medium and would be present in an otherwise ideal polarimeter, discussed in the present section, and those that depend on non-ideal properties of the polarimeter, which will be discussed in Sec. VI B. The expected size of systematic effects from the first class can be calculated analytically or simulated by Monte Carlo given the properties of the medium, the geometry, and the neutron optical properties of the apparatus. Systematic uncertainties of the second class can depend on nonuniformities in the phase space properties of the neutron beam which couple to other asymmetries in the apparatus in a way that is difficult to characterize analytically. It is clear that subsidiary measurements to address these latter effects must be performed. We performed these measurements and described them in detail in an earlier paper.[38] We placed upper bounds on possible systematic effects *in situ* by amplifying the size of any effects coupled to internal magnetic fields by running with amplified internal fields. We summarize the results in Sec. VI C. Finally we analyzed the experimental data with the π-coil off. We discuss the procedure employed to perform this analysis in Sec. VI D.

Sources of systematic effects present even in the ideal case of uniform neutron beam phase space properties include: the diamagnetism of the medium, the neutron optical potential of the medium, the shift in the neutron energy spectrum due to energy-dependent neutron scattering in the medium coupled with possible target length differences, small angle neutron scattering in the medium, and multiple scattering in the medium.

1. Diamagnetism

The presence of the medium modifies the size of the residual magnetic field through its diamagnetism, thereby changing the neutron spin rotation from the residual magnetic field in the volume of space it occupies as the target is moved in and out of a given volume. The change in the rotation angle can be calculated from Eq. (25) using the value for the volume magnetic susceptibility of the material and the size of the field in the target. For example, in the particular case of helium which has a volume magnetic susceptibility of $\chi_v = -1.89 \times 10^{-6}$ cc/mole,[39] the resulting shift $\frac{\delta B}{B} = 4\pi\chi_v = -1 \times 10^{-6}$ gives a -2×10^{-9} rad effect for slow neutrons in a 1 m target. This effect could be larger for many other substances, but as long as the medium does not possess magnetic order, this shift is typically much smaller than the 1×10^{-7} rad/m goal for most materials.

2. Neutron optical potential

The presence of the target medium slows down the neutron beam, whose polarization therefore precesses more in

the residual magnetic field than with the empty target. The neutron optical potential of matter is typically ≈100 neV. The kinetic energy of the neutron beam averages about 3 meV for a wavelength of 5 Å. The fractional change in neutron velocity with and without the medium therefore leads to a systematic effect of about 1×10^{-8} rad at 5 Å. Again this is an order of magnitude smaller than the sensitivity goal of interest. Note that the sign of this effect depends on the sign of the neutron optical potential and would be different for materials like hydrogen and titanium, which have negative values for the neutron optical potential.

3. Shift in neutron energy spectrum due to scattering coupled with target length differences

The neutron scattering cross section of the target medium will in general vary over the energy spectrum of a cold neutron beam used in the experiment. Therefore, the average neutron velocity is slightly shifted after passing through the target as different velocity classes are removed from the beam according to the transmission law $T = \exp[-n\sigma(E)t]$, where n is the target number density, $\sigma(E)$ is the total neutron cross section for neutrons of energy E, and t is the target length. The size of the shift is greater for a longer target. Therefore, for targets of different lengths, this difference in average velocity, coupled with a difference in residual magnetic field in the two target regions, gives a systematic effect. The energy dependence of the total neutron cross section over the cold neutron beam spectrum typically possesses a rapid variation as the neutrons pass through either the Bragg cutoff energies (for solids) below which diffraction turns off or below neutron wavelengths corresponding to the atomic separation (for liquids) below which one gets destructive interference in the scattering from neighboring atoms. This change in the total neutron cross section can be as much as a factor of 2 over an energy range of a few meV. $\frac{\delta v}{v} \approx 0.05$ is a typical value for this effect in a target whose length has been chosen to optimize the signal size according to the considerations presented in Sec. III. Assuming a length mismatch of $\frac{\delta L}{L} = 10^{-4}$ (achieved in our liquid helium target using standard machining techniques) gives a 1×10^{-8} rad systematic effect. This effect could be larger at higher neutron energies for targets made of heavy nuclei, which possess sharp compound nuclear resonances and therefore a very rapid cross section change over a small energy interval. Sharp compound nuclear resonances in the slow neutron energy range of interest for this paper are relatively sparse. This systematic uncertainty obviously goes away if instead one mechanically moves a solid target in front of and behind the π-coil as was done in many of the original spin rotation measurements.

4. Small angle neutron scattering in the target

In addition to the neutrons which pass straight through the target, there are some neutrons that scatter, elastically or inelastically, through small angles within the phase space acceptance of the polarimeter. The spin rotation angle of these scattered neutrons which reach the analyzer and then the detector can differ for the two target positions for several reasons (solid angle differences, magnetic field gradients, differences of the dwell time of the scattered neutrons in the field, etc.) and can lead to a systematic effect.

Fortunately, small angle scattering intensity in condensed media in thermodynamic equilibrium can be calculated using general results from thermodynamics and hydrodynamics in the small momentum transfer regime of relevance for this potential source of systematic uncertainty. For $qa \ll 1$, where a is the atomic separation, the fluctuation-dissipation theorem can be used to relate the spectrum of equilibrium density fluctuations to the thermal and continuum properties of the medium. In this limit, there is a universal form for both the static structure factor $S(q)$ and the dynamic structure factor $S(q,\omega)$ of a liquid at finite temperature and therefore the differential and double differential cross sections $\frac{d\sigma}{d\Omega}$ and $\frac{d^2\sigma}{d\Omega dE}$, respectively.[40–43] The dynamic structure factor $S(q,\omega)$ is proportional to the probability that an incident neutron transfers momentum $\hbar q$ and energy $\hbar\omega$ to the scatterer in one collision. The double differential cross section $\frac{d\sigma}{dEd\omega}$ is directly proportional to the dynamic structure factor $S(q,\omega)$,

$$\frac{d^2\sigma}{dEd\Omega} = b^2\frac{k}{k_0}S(q,\omega), \tag{33}$$

where b is the scattering length for a bound atom and k and k_0 are the wave numbers for the scattered and incident neutrons.

For the neutron small angle scattering intensity, $\lim_{q\to 0} S(q) \to \frac{\hbar q}{2mv_s}\coth\frac{\hbar v_s q}{2T}$, where v_s is the velocity of sound, m is the mass of the atom, and T is the temperature of the medium. For $\frac{\hbar v_s q}{2T} \ll 1$, $\lim_{q\to 0} S(q) \to \frac{T}{mv_s^2} = \frac{c_v}{c_p}\rho\kappa T$, where c_p and c_v are the specific heats at constant pressure and constant volume, ρ is the density, and κ is the isothermal compressibility. This gives rise to a differential cross section $\lim_{q\to 0}\frac{d\sigma}{d\Omega} \to \frac{\sigma}{4\pi}\frac{c_v}{c_p}\rho\kappa T$, where σ is the bound neutron-atom cross section.[40] This result indicates that it is useful to maintain the target medium at low temperature to reduce small angle scattering from thermally excited density fluctuations in the medium. For a ratio of specific heats at constant pressure and constant volume $\frac{c_p}{c_v} \approx 1$, this expression reduces to the well-known result for a classical liquid: $\lim_{q\to 0} S(q) \to \rho\kappa T$.[41]

Away from the $q \to 0$ limit, one can also calculate $S(q,\omega)$ and the relative intensities of the elastic and inelastic components of small angle scattering from condensed media in the hydrodynamic regime. The elastic and inelastic components come from scattering due to diffusive and sound modes, respectively, and are therefore the neutron equivalent of the famous Rayleigh and Brillouin peaks in light scattering. The detailed expression for $S(q,\omega)$,[42]

$$S(q,\omega) = \frac{2k_BT}{mc_t^2}\Big[\frac{c_v}{c_p}\frac{D_Lc_s^2q^4 - q^2(\omega^2 - c_s^2q^2)D_T(\frac{c_p}{c_v}-1)}{(\omega^2 - c_s^2q^2)^2 + (\omega q^2D_L)^2)} + (1-\frac{c_v}{c_p})\frac{q^2D_T}{\omega^2 + (D_Tq^2)^2}\Big], \tag{34}$$

has three peaks: the central quasielastic Rayleigh component and the two Brillouin doublets at frequencies $\omega = \pm c_sq$ corresponding to the sound velocity. In this equation, c_T is the isothermal sound velocity, $c_s = \sqrt{\frac{c_p}{c_v}}c_T$ is the adiabatic sound velocity, and $D_T = \frac{\kappa}{\rho c_p}$ and $D_L = D + (\frac{c_p}{c_v} - 1)D_T$ determine

the half-widths of the Rayleigh and Brillouin peaks, with D the diffusion coefficient. As follows from the above formula, there is a well-known expression for the relative intensities of the quasielastic Rayleigh peak and the inelastic Brillouin peaks: $\frac{I_R}{2I_B} = \frac{c_p - c_v}{c_v}$.[43]

We use liquid helium as an example. Figure 11 shows $S(\omega)$ plots at various q values. The central peak centered at $q = 0$ and $\omega = 0$ corresponds to quasi-elastic scattering from diffusive motion of the atoms in the liquid, whereas the peaks at $\omega = cq$ with c the velocity of sound correspond to creation and absorption of one phonon in the liquid. For energy and momentum transfers small enough to fall within the hydrodynamic regime, the relative intensities of the three peaks are set by thermodynamics. The intensity of the quasi-elastic peak in helium is consistent with X-ray scattering measurements[44] of the static structure factor $S(q)$ extrapolated to the $q \to 0$ limit. The relative intensity of the three peaks and the equality of the intensity of the phonon creation and absorption peaks have been verified in light scattering experiments in liquid helium between 2 and 4 K[45,46] and are also expected on physical grounds. Since the energy associated with the 4 K liquid temperature $k_B T \gg \hbar\omega$ is greater than the small energy transfers involved in the small angle scattering, the detailed balance factor $\exp \frac{\hbar\omega}{k_B T}$, which relates the relative probabilities of scattering with energy gain (upscattering) and energy loss (downscattering), approaches unity.

Using these expressions, we can therefore estimate the small angle scattering systematics in liquid helium as follows. For elastic small angle scattering, based on the neutron cross sections, 1 m liquid helium target length, and phase space acceptance of the 1 m long glass output guide, a fractional difference of 10 ppm of the neutrons scatter from the two target positions into the polarimeter and the glass output guide. The extra spin rotations in the residual magnetic field then produce a systematic effect of 5×10^{-9} rad. For the inelastic small angle scattering from sound waves in helium, the total intensity of the scattering is the same as for the elastic scattering from experiment as noted above, and at 4 K, it is equally split between energy gain and energy loss. Therefore, the size of the systematic effect is about the same as for the small angle elastic scattering, namely, 5×10^{-9} rad. This is comparable to the scale of the other systematic uncertainties mentioned

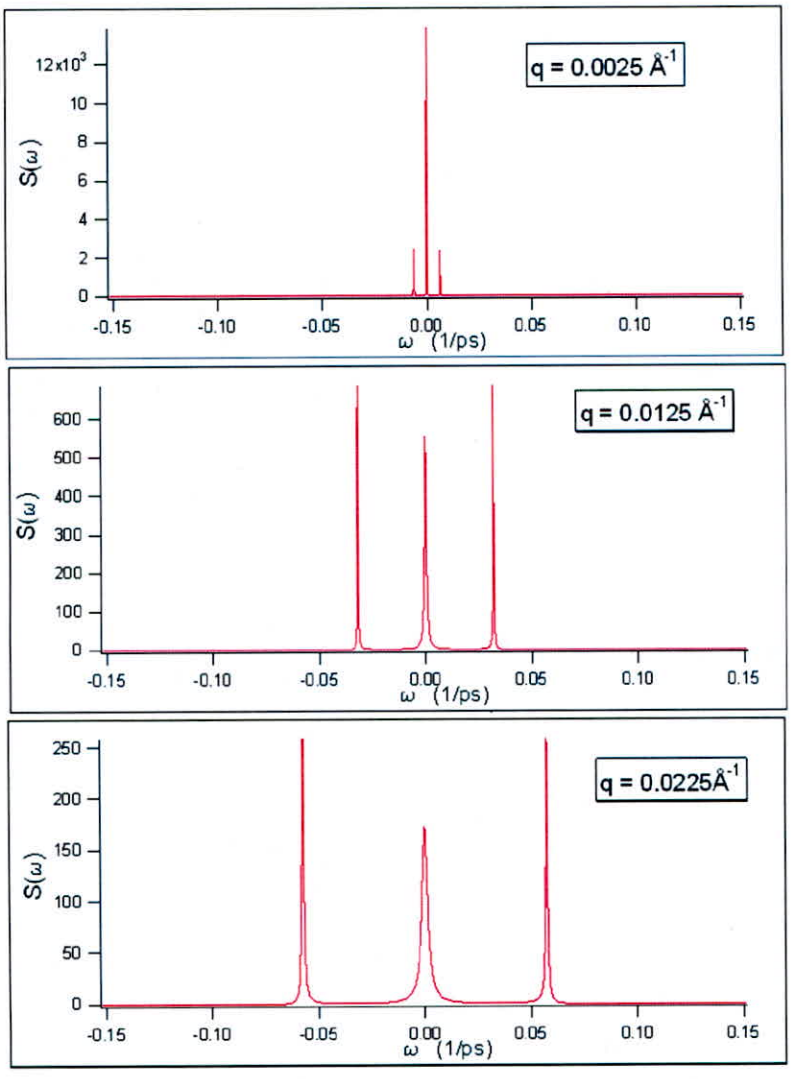

FIG. 11. $S(\omega)$ plots at various q values.

above. For other materials, the optimum target thicknesses are about an order of magnitude smaller than for liquid helium, and generically this much shorter target length and smaller difference in the fraction of small angle scattered neutrons accepted into the downstream polarimeter will further suppress this systematic by another order of magnitude.

5. Multiple scattering in the target

There are also neutrons which can multiple scatter in the target and enter the detector. The extra dwell time of the neutron in the residual field from multiple scattering can in principle give a systematic effect. For solid targets, the Bragg scattering from crystallites can give a nontrivial probability for multiple scattering back into the forward direction, and previous experience with neutron spin rotation measurements shows that this is not a negligible systematic effect for typical crystallite sizes and distributions in polycrystalline solids. For this reason, some of the previous spin rotation measurements were forced to restrict the incoming neutron spectrum to wavelengths beyond the Bragg cutoff of the solid target material to avoid diffraction completely.

Although there is no Bragg scattering in a liquid, there is still multiple scattering. Calculations and measurements of the angular distribution of the scattering of slow neutrons in materials show that it has both significant neutron energy and temperature dependence. The rapid energy dependence of scattering in this energy and momentum transfer regime is a result of destructive interference in the scattering from neighboring atoms. The fraction of multiply scattered neutrons that make it into the polarimeter is dominated by the target geometry and polarization analyzer phase space acceptance and is further suppressed by the ratio of the width of the neutron beam to the length of the target. In our helium target, we estimate that a fraction of about 2×10^{-5} of the neutrons multiple scatter into the acceptance of the output guide and analyzer and that the average difference in the neutron spin rotation angles for the multiply scattered neutrons from the front and back targets is about 0.2 mrad, again mainly determined by geometry. This gives a 4×10^{-9} systematic effect for our liquid helium target. It would be comparable for most other substances: although the neutron scattering cross sections are typically somewhat larger, this is more than compensated by the smaller target lengths for optimized transmission and therefore the smaller differences between the extra neutron rotation angles for the two target positions.

6. Large target nonuniformities

For either liquids or solids, density nonuniformities will increase the small angle scattering intensity from the estimates described earlier. We first focus on large nonuniformities. For liquids, bubbles are possible. Polycrystalline solids can produce extra small angle scattering from density nonuniformities due to grain boundaries, internal stress, etc. Since these possible effects are not easy to estimate, the main strategy to eliminate this class of possible systematic effects is to ensure that these nonuniformities are either absent (in the case of bubbles) or static (in the case of cracks and voids in solids).

Bubbles are a possible concern both for increased systematic effects due to extra small angle scattering and also for the possibility of increased statistical noise in the measurement from density fluctuations as mentioned earlier. In fact, bubbles in boiling liquids have been measured in the past using slow neutron transmission.[57,58] The agreement between the statistical accuracy of the measurement in liquid helium and the estimate expected from neutron counting statistics discussed in Sec. V can be used to place an upper bound on the fraction of target volume occupied by bubbles. However, although it is possible to calculate the neutron small angle scattering from spherical bubbles reliably, it is not easy to predict the density and size distribution in a realistic target, which depends in detail on the size of temperature gradients, the nature of surface conditions, and the properties of the liquid. Several things are known experimentally from the numerous studies that have been performed of bubble formation and dynamics in liquid helium for cryogenic engineering and in liquid hydrogen for bubble chambers used in high energy physics experiments.[47–52] From these studies, it is known experimentally that the rate of production of bubbles typically increases exponentially for heat fluxes beyond a certain threshold, and so, an isothermal target with negligible heat influx should possess few if any bubbles.

The best experimental solution to suppress bubble formation is to operate the liquid in a slightly supercooled state to render the growth of bubbles thermodynamically unfavorable. This was done in the liquid helium target by measuring the target temperature and controlling the pressure of the boiloff gas from the evaporating liquid at a location far away from the liquid in the target to be higher than the equilibrium vapor pressure corresponding to the target temperature. This can be done by exploiting the finite thermal conductivity of the tube through which the boiloff gas evaporates. This technique is also employed successfully in liquid hydrogen targets which are capable of absorbing a few hundred watts of power while still maintaining density fluctuations small enough to successfully perform sub-ppm precision parity violation experiments in polarized electron scattering experiments.[53–56]

7. Target-dependent neutron optical effects

First, we consider the bending of neutron trajectories from gradients in the neutron optical potential due to gradients in target density. The latter can come from several possible effects such as gravity, pressure and temperature fluctuations, and static density nonuniformities in a solid. In a mechanism similar to that for the small angle scattering systematics described above, the time that the polarized neutrons in such bent trajectories spend in the residual field will be different for the two target positions and a different fraction of these trajectories will be accepted by the analyzer, and in principle, this combination can generate a systematic effect.

We estimate the typical size of such effects by assuming a gradient of the neutron index of refraction in the target over a certain length and calculating the change in direction of the transmitted neutron trajectory from neutron optics. As an example, we estimate the angular deflection of the cold neutron beam in liquid helium due to the gravity-induced

density change, which is of order $\theta = \frac{\delta p}{p} = \frac{l}{2}\frac{dV_{opt}}{dx}\frac{1}{E_k}$, where E_k is the neutron kinetic energy and $\frac{dV_{opt}}{dx}$ is the gradient in the neutron optical potential transverse to the direction of neutron motion. For liquid helium, the liquid pressure changes by 10^{-3} over the height of the liquid in the beam, which gives a change of 10^{-3} of the liquid density and therefore of the neutron optical potential. Such a fractional change in the 10 neV neutron optical potential of liquid helium acting over the 0.5 m target length bends the neutron beam up by an average angle of $\approx$30 nrad and therefore a $\approx 10^{-10}$ difference in the spin rotation angles accepted by the polarimeter in the two target states. Other liquid targets composed of material with larger neutron optical potentials might increase the size of this effect by an order of magnitude.

Target-dependent shifts in the phase space of the beam from refraction effects are minimized by making the boundaries of all surfaces normal to the mean beam momentum. Since all neutron optical boundaries seen by the forward-going beam are normal to the neutron momenta, first-order effects from neutron refraction-induced changes in the neutron paths are suppressed. Typical transverse neutron beam motion and angle shifts with the introduction of the liquid assuming typical manufacturing tolerances for the chambers and typical alignment accuracies of the mean neutron beam momentum with the target boundaries are of order 10^{-2} μm and 1 μrad, respectively, and it is the difference in these numbers for the two targets coupled with the residual field which is needed to generate a systematic effect.

An important neutron optical systematic effect at the edges of phase space acceptance can come from neutron reflection from the walls of the target. Since the critical angle for reflection is slightly different for a solid-liquid interface and a solid-gas interface and in both cases these angles can both fall within the phase space acceptance of the polarimeter given the typical critical angles for neutron reflection from material boundaries, any change in the residual magnetic field seen by the neutrons close to the edges of the beam can lead to a systematic effect. Consider a specific case. The neutron optical potential of aluminum is 54 neV and the neutron optical potential of liquid helium is 10 neV; the difference in the critical angle for reflection from the two interfaces for a 5 Å neutron is 0.4 mrad and the fraction of the beam that can be affected by this reflection is 1×10^{-5}. This possible systematic effect can be reduced significantly by introducing baffles into the target chamber to exclude wall-reflected neutrons from the phase space acceptance of the analyzer. This suppresses the effect by at least the ratio of the total thickness of the baffles to the length of the target chamber, which is about 0.6 cm/50 cm $\approx 10^{-2}$, and in reality, this suppression will be much greater due to the large neutron absorption of the baffle material and the roughness of the surface it presents. Assuming a 10 nT field as above gives a 2×10^{-10} systematic effect.

8. Nonforward scattering coupled to gradients in the axis of the field of the output coil

The output coil adiabatically transports the projection of the neutron polarization onto the axis of its magnetic field direction just after the polarized neutrons cross into the coil through the non-adiabatic entrance into the coil. If the output coil field axis has gradients transverse to the direction of the neutron beam and the non-forward scattered neutrons sample slightly different spatial areas of the beam, then there will be a target-dependent difference in the rotation angles seen in the polarization analyzer which causes a systematic effect.

The size of this possible effect can be estimated as follows. The fractional difference of the nonforward scattered neutrons which get to the polarization analyzer is of order 10^{-5}. The rotation angles possessed by these neutrons at the entrance to the output coil are typically 5 mrad for a 100 μG internal field and the typical difference in spatial location of the nonforward-scattered neutrons projected onto the entrance to the output coil is about 2 mm. Even a large gradient in the direction of the field of 10% over this distance would give a systematic effect of only 5×10^{-10}. We conclude that this potential source of systematic error can be made negligible by proper design of the fields of the output coil.

B. Sources of systematic uncertainty from instrumental imperfections

All of the systematic effects outlined above are present under the assumptions of a uniform-wavelength beam distribution, uniform intensity across the beam, uniform analyzing power of the analyzer within its phase space acceptance, and a cylindrically symmetric residual magnetic field inside the apparatus. If one relaxes these assumptions, then one immediately encounters another large possible set of systematic effects which are associated with various possible correlated products of nonuniformities in the phase space properties of the beam, apparatus, and target. It is not possible to predict these potential systematic effects without a detailed knowledge of the variation of the phase space properties of the beam and the polarimeter. So, it is essential to measure the typical size and length scale for the variation of these phase space nonuniformities experimentally.

These measurements were performed and described in detail in previous work.[38] We can set the scale for the typical uniformity requirements for certain phase space properties of the beam as follows. For a 10 nT residual field which rotates the typical cold neutron by an angle of a few milliradians, we need to limit the product of all of these nonuniformities which change the transmission intensity through the polarization analyzer at the 10^{-5} level as mentioned earlier in this section. Due to the split beam, one needs a product of more than one of these nonuniformities to generate a systematic effect. This means that we are interested in constraining the fractional nonuniformities of certain beam, target, or polarimeter properties at the 10^{-2} to 10^{-3} level. Furthermore, since the fraction of non-forward scattered neutrons from the liquid helium accepted by the polarimeter is at the $\approx$100 ppm level and we have already estimated the systematic effects associated with these sources earlier, we can concentrate the rest of our analysis on effects which act on the unscattered beam. These include variations in transmission due to possible large target nonuniformities such as bubbles or voids and variations from small target nonuniformities such as gradients in density. By definition, the latter effects fall within the regime of

description for neutron optics and can therefore be analyzed in a straightforward manner. It is clear that we must be especially careful about those properties of the beam that are influenced by the target and are close to the edge of the acceptance of the polarimeter in any phase space variable, because this is where the fractional changes can be large.

The measurements performed and described in Ref. 38 combined with relatively simple calculations involving the transmitted beam place an upper bound of 1×10^{-8} rad on possible systematics from polarimeter nonuniformity and 6×10^{-8} rad on a possible correlated nonuniformity of the target and the polarizing and analyzing power of the polarimeter. These small effects were measured despite the use of a highly nonideal neutron polarization analyzer which possessed major nonuniformities in its analyzing power in phase space. These effects can be further suppressed using modern polarized neutron optics technology.

C. Bounding systematic effects through auxiliary measurements

It is essential to have a strategy to amplify experimentally possible systematic effects and either isolate and eliminate them or place upper bounds on their size. One can place upper bounds on such possible systematic effects. For all systematic effects which couple to internal magnetic fields or internal magnetic field gradients, one conducts measurements in which the internal magnetic field and the internal magnetic field gradients are increased well above the running conditions of the experiment. This amplifies all magnetic field-induced systematic effects (which constitute the great majority of the effects discussed above) by the same factor and makes it possible to find or bound such effects in a time short compared to the measurement time. This procedure works under the assumption that we can scale the upper bound by the ratio of the fields/field gradients present in the auxiliary measurement and the production data. This is a good assumption as even the larger fields used to amplify the possible scattering systematic effects are still small enough (of order 1 μT) that they do not affect the rest of the polarimeter.

As an example, in our liquid helium experiment, two measurements were conducted: one with a (relatively) large constant longitudinal field in the same direction in both target chambers and another with a large upstream/downstream magnetic field gradient in the target region with the longitudinal fields in opposite directions in the two target chambers. Both fields were produced by running appropriate currents through the trim coils wrapped around the target insert. The current going through the trim coils was setup symmetrically upstream and downstream of the π-coil with opposite signs for the gradient field and the same signs for the constant field. The fields inside the target were measured by the fluxgate magnetometers immediately before the data were taken.

Figure 12 shows the data taken with a magnetic field 100 times the size of the residual field present in the main experiment. We also took data with liquid helium placed in a longitudinal magnetic field gradient chosen to be positive in the upstream target region and negative in the downstream target region with a magnitude larger than the gradients present in the experiment by a factor of 100. All these data are consistent with zero parity-odd asymmetry within the statistical error. Using these measurements we place an upper bound of $<4 \times 10^{-8}$ rad on any systematic effects coupled to longitudinal magnetic fields and an upper bound of $<3 \times 10^{-8}$ rad from magnetic field gradients for the conditions of the experiment.

Likewise to set an upper bound on all systematic effects associated with possible target-dependent nonuniformities in the polarization products of the polarimeter, we set the polarimeter output angle to extreme values to amplify these possible systematics. An example of a systematic effect of this type is a target-dependent east-west polarimeter analyzing power differences. It is a "triple conspiracy" systematic proportional

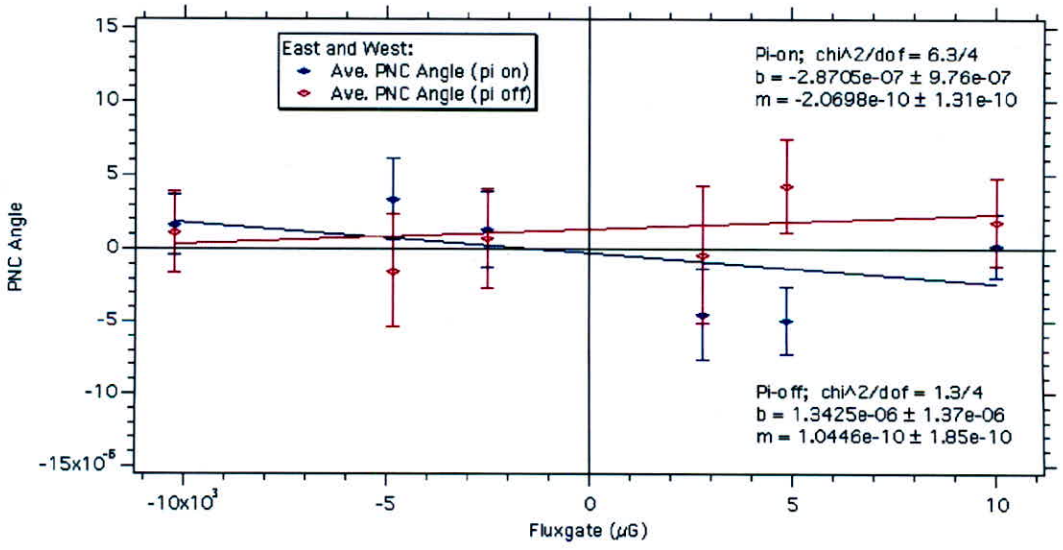

FIG. 12. Measurements of the parity-odd neutron spin rotation angle in the presence of amplified longitudinal magnetic fields. The plot shows data taken with liquid helium placed in a longitudinal magnetic field of 0, ± 0.5 μT, and ± 1 μT. These data amplify any systematic effect coupled to the total line integral of the magnetic field in the target region by a factor of 100.

to $[(PA_W - PA_E)_{T0} - (PA_W - PA_E)_{T1}]\phi$, where PA_W and PA_E are the west and east PA products of the polarimeter, $T0$ and $T1$ are the transmitted intensities in the two target states, and ϕ is the measured spin angle under these conditions. This was done by placing the polarization analyzer angle at much larger values than normally used in the experiment. The upper bound on this possible systematic of 6×10^{-8} rad/m we achieved for the liquid helium target is consistent with the upper bounds on this systematic set before by the measurements of the polarimeter properties referred to above.

As another internal check on the consistency of these upper bounds on systematic uncertainties, one can observe the east-west asymmetry in the intensity differences between the two target states. These measurements give us another experimental handle on possible systematic effects due to nonforward scattering. The fractional difference in the transmitted intensity through the polarimeter in the two target states directly measures the difference in the nonforward scattering in the two target positions with the relevant weighting of elastic and inelastic small angle scattering, multiple scattering, differential neutron spectrum changes, and any other possible neutron refraction effects that enter the polarimeter, thereby subsuming many of the individual systematic effects discussed above. The product of this asymmetry with the asymmetry in the spin rotation angle from residual fields in the two target positions can place an experimental upper bound on systematic effects from nonforward scattering.

Table II shows a summary of the size of various contributions to the systematic uncertainty under the assumptions stated above. The calculated systematic effects for a liquid helium target are well below 10^{-7} rad/m. The measured upper bounds on the systematic effects added in quadrature are 1.4×10^{-7} rad/m.

D. Systematic uncertainty measurement from the π-coil off data

Finally, one can measure the systematic uncertainty during the measurement using the π-coil off data. As mentioned in Sec. II, with the π-coil off the asymmetry must be zero in the absence of systematic uncertainties. The π-coil off measurement is interleaved into the standard data taking protocol and therefore is the most direct method to measure the systematic uncertainty.

To convert a nonzero measurement of a π-off asymmetry into a systematic uncertainty on the neutron rotary power, one must know the appropriate conversion factor between the two. This can be determined from the measurement of the polarizer-analyzer product PA described in Sec. III B in Eqs. (27) and (28). In the presence of internal magnetic fields, however, the measured PA values of relevance correspond to neither PA^π nor PA^0 defined above: instead, PA^π is in fact a linear combination of PA^π and PA^0. This is because the horizontal component of any precession angle that occurs upstream of the π-coil both changes sign and is reduced by the factor d, whereas the measured asymmetry after passing through the rest of the target includes both this contribution added to any additional precession from the downstream side of the coil. The PA product for the east and west sides in the presence of internal longitudinal fields is therefore given by

$$\begin{aligned} \mathcal{A}^\pi(x) &= PA^0(1 - (1+d)x)\sin\phi \\ &= PA^x \sin\phi, \end{aligned} \tag{35}$$

where x is the fraction of the total rotation angle that occurred upstream of the π-coil, and d is the factor by which the π-coil over-rotates or under-rotates the neutron spin, averaged over the wavelength spectrum. PA^x is the π-coil on product in the presence of magnetic fields and it is the quantity needed to properly normalize any observed π-off asymmetry in terms of a systematic uncertainty on the parity-odd spin rotation angle.

The π-coil is at the geometrical center of the target, so for a uniform longitudinal B field with $x = 1/2$, and $d \approx 0.6$ from Fig. 8, π-on asymmetries from magnetic rotations are reduced by a factor of 5 compared with π-off asymmetries. However, the internal magnetic field is neither uniform nor exactly constant from run to run and it is not possible to determine x from the internal magnetometer measurements alone. Nevertheless, x can be determined by comparing the total integral of the magnetic field in the target region as inferred from the calibrated ion chamber signal described earlier with the measurements of the internal magnetic field at certain points in the target region from the fluxgate magnetometer.

TABLE II. A list of sources for potential systematic effects and estimates for the uncertainties for the specific case of liquid helium compared to the upper bound from auxiliary measurements. The measured upper bounds on the systematic effects are consistent with the calculated estimates.

Source	Uncertainty (rad/m)	Method
Liquid ^{4}He diamagnetism	-2×10^{-9}	calculated
Liquid ^{4}He optical potential	$+3\times10^{-9}$	calculated
Neutron E spectrum shift	8×10^{-9}	calculated
Neutron refraction/reflection	3×10^{-10}	calculated
Nonforward scattering	2×10^{-8}	calculated
Polarimeter nonuniformity	1×10^{-8}	measured
B amplification	$<4\times10^{-8}$	measured
B gradient amplification	$<3\times10^{-8}$	measured
PA/target nonuniformity	$<6\times10^{-8}$	measured
Total (upper bound, from measurements)	1.4×10^{-7}	

Thus, the extraction of the systematic uncertainty from the experimental data proceeds through the following steps. First, we isolate the contributions to the total spin rotation angle from different sources. Then, we use the ion chamber calibration of the sensitivity of the polarimeter to longitudinal magnetic fields along with the measurements of the polarization products for the two sub-beams in the apparatus to experimentally determine the degree of common-mode suppression of the spin rotation from internal magnetic fields using the π coil off data with a known amplified internal magnetic field. We multiply this suppression factor with the value of the average magnetic field as determined from the ion chamber response to extract the systematic uncertainty. The details of how these analysis procedures are implemented in practice will appear in a forthcoming paper on the results of the liquid helium measurements.

VII. CONCLUSION

In this paper, we have presented the design, performance, and an outline of the statistical and systematic uncertainty analysis for an apparatus which is capable of measuring the rotary power for polarized slow neutrons passing through matter at the level of $d\phi/dz = 1 \times 10^{-7}$ rad/m. Our apparatus is optimized to measure a very small rotation angle with an accuracy of a few percent and a high insensitivity to possible sources of systematic uncertainty. A new phase of the liquid helium measurement which motivated the development of this apparatus is planned[8] at a more intense neutron beam under construction at NIST[59] which should have enough neutron flux to conduct a measurement with this statistical precision.

The same methods we have described here could also be used to measure the neutron rotary power in other target media. Although our work has been mainly motivated by the search for neutron-nucleus parity violation from the electoweak sector of the Standard Model and by searches for possible exotic sources of neutron parity violation, there are many other ways that condensed media can generate mirror-asymmetric interaction of polarized neutrons in the medium which this apparatus could be used to measure. Examples include, but are not limited to, neutron spin rotation in handed molecules,[60–62] noncentrosymmetric perfect crystals,[63–67] materials with helical internal magnetic fields,[68] and spinning matter.[69–71] A slightly modified apparatus configuration with the π-coil after a target split into quadrants is now in preparation for a proposed search for possible exotic parity-even neutron spin-dependent interactions[72,73] which can cause transversely polarized neutrons to tilt forward rather than to rotate relative to the beam momentum.

The specific apparatus, measurement method, and systematic effect analysis described in this paper is best suited to media which do not possess or produce magnetic fields. However, the systematic effects for measurements of neutron spin rotation in media such as polarized targets and magnetized materials are broadly similar, and many of the same considerations described in this paper also apply. Examples include polarized neutron techniques such as spherical neutron polarimetry[74–76] and experiments envisioned for possible tests of time reversal invariance in epithermal polarized neutron transmission through polarized nuclear targets.[77,78] A description of methods which can be used to further improve the precision of neutron polarimetry in these systems as well would be very useful.

ACKNOWLEDGMENTS

This work was supported in part by NSF PHY-0457219, NSF PHY-0758018, DE-AI02-93ER40784, DE-SC0010443, DE-FG02-95ER40901, and UNAM Grant No. PAPIIT-UNAM IN111913. We acknowledge the support of the National Institute of Standards and Technology, US Department of Commerce, in providing the neutron facilities used in this work. H. Gardiner, D. Esposito, and J. Lieffers acknowledge support from the NSF Research Experiences for Undergraduates program NSF PHY-1156540. W. M. Snow, E. Anderson, J. Fry, C. Haddock, and A. T. Holley acknowledge support from the Indiana University Center for Spacetime Symmetries.

[1]V. G. Baryshevshy, *High Energy Nuclear Optics of Polarized Particles* (World Scientific, 2012).
[2]F. C. Michel, Phys. Rev. **133**(2B), B329 (1964).
[3]L. Stodolsky, Phys. Lett. B **50**, 353 (1974).
[4]P. S. Farago, J. Phys. B: At. Mol. Phys. **14**, L743 (1981).
[5]W. M. Snow *et al.*, Phys. Rev. C **83**, 022501(R) (2011).
[6]H. Yan and W. M. Snow, Phys. Rev. Lett. **110**, 082003 (2013).
[7]R. Lehnert, W. M. Snow, and H. Yan, Phys. Lett. B **730**, 353 (2014).
[8]W. M. Snow *et al.*, Nuovo Cimento C **35**, 57 (2012).
[9]M. Forte *et al.*, Phys. Rev. Lett. **45**, 2088 (1980).
[10]B. R. Heckel *et al.*, Phys. Lett. B **119**, 298 (1982).
[11]B. R. Heckel *et al.*, Phys. Rev. C **29**, 2389 (1984).
[12]S. Saha, Ph.D. thesis, University of Washington, 1990.
[13]I. B. Khriplovich, *Parity Nonconservation in Atomic Phenomena* (Gordon and Breach, 1991).
[14]A. P. Serebrov, A. K. Petukhov, G. V. Valskii, G. A. Petrov, and Yu. S. Pleva, JETP Lett. **62**, 529 (1995).
[15]K. Sakai *et al.*, Phys. Lett. B **391**, 11 (1997).
[16]W. Heil, K. Andersen, D. Hofmann, H. Humblot, J. Kulda, E. Lelievre-Berna, O. Scharpf, and F. Tasset, Physica B **241-243**, 56 (1998).
[17]T. Haseyama *et al.*, Phys. Lett. B **534**, 39 (2002).
[18]B. Heckel *et al.*, J. Phys. Colloq. **45**(C3), 89 (1984).
[19]C. D. Bass *et al.*, Nucl. Instrum. Methods Phys. Res., Sect. A **612**, 69 (2009).
[20]W. M. Snow, Nucl. Instrum. Methods Phys. Res., Sect. A **611**, 248 (2009).
[21]D. Markoff, Ph.D. thesis, University of Washington, 1997.
[22]L. Koester and A. Steyerl, *Neutron Physics* (Springer Verlag, 1977).
[23]M. L. Goldberger and K. M. Watson, *Collision Theory* (John Wiley, 1964).
[24]D. J. Hughes, *Neutron Optics* (Interscience Publishers, Inc., 1954).
[25]F. Mezei, Z. Phys. **255**, 146 (1972).
[26]L. Van Hove, Phys. Rev. **95**, 249 (1954).
[27]W. Marshall and S. W. Lovesey, *Theory of Thermal Neutron Scattering* (Clarendon Press, Oxford, 1971).
[28]R. Gahler, J. Felber, F. Mezei, and R. Golub, Phys. Rev. A **58**, 280 (1998).
[29]R. Gahler, R. Golub, K. Habicht, T. Keller, and J. Felber, Physica B **229**, 1 (1996).
[30]H. E. Swanson and S. Schlamminger, Meas. Sci. Technol. **21**, 115104 (2010).
[31]S. Penn *et al.*, Nucl. Instrum. Methods Phys. Res., Sect. A **457**, 332 (2001).
[32]J. D. Bowman and J. C. Vanderleeden, Nucl. Instrum. Methods **85**, 19 (1970).
[33]J. S. Nico *et al.*, J. Res. Natl. Inst. Stand. Technol. **110**, 137 (2005).
[34]O. Schaerpf, Physica B **156-157**, 631 (1989); **156-157**, 639 (1989).
[35]M. Forte, *Fundamental Physics with Reactor Neutrons and Neutrinos*, American Institute of Physics Conference Series Vol. 42, edited by T. Von Egidy (Taylor & Francis, 1978), p. 80.
[36]J. Als-Nielsen and O. Dietrich, Phys. Rev. **133**, B925 (1964).
[37]C. D. Keith *et al.*, Phys. Rev. C **69**, 034005 (2004).
[38]A. Micherdzinska *et al.*, Nucl. Instrum. Methods Phys. Res., Sect. A **631**, 80 (2011).

[39]R. E. Glick, J. Phys. Chem. **65**, 1552 (1961).
[40]W. Marshall and S. W. Lovesey, *Theory of Thermal Neutron Scattering* (Oxford University Press, 1971), Chap. 12.
[41]L. S. Ornstein and F. Zernicke, Z. Phys. **19**, 134 (1918).
[42]N. H. March and M. P. Tosi, *Atomic Dynamics in Liquids* (John Wiley, 1976).
[43]L. D. Landau and G. Placzek, Phys. Z. Sovjetunion **5**, 172 (1936).
[44]H. N. Robkoff and R. B. Hallock, Phys. Rev. B **24**, 159 (1981).
[45]G. Winterling, F. S. Holmes, and T. J. Greytak, Phys. Rev. Lett. **30**, 427 (1973).
[46]W. F. Vinen, Philos. Trans. R. Soc., A **293**, 377 (1979).
[47]B. Louie and W. Seward, Adv. Cryog. Eng. **35**, 403 (1990).
[48]G. Harigel, Nucl. Instrum. Methods Phys. Res., Sect. A **421**, 12 (1999).
[49]M. Tate and M. Sadler, Nucl. Instrum. Methods Phys. Res. **204**, 295 (1983).
[50]T. Dombeck and J. Vanhoy, Nucl. Instrum. Methods **177**, 347 (1980).
[51]G. Harigel, H. Hilke, G. Linser, and F. Schenk, Nucl. Instrum. Methods Phys. Res. **188**, 517 (1981).
[52]G. Horlitz, S. Wolff, and G. Harigel, Nucl. Instrum. Methods **117**, 115 (1974).
[53]E. J. Beise, D. H. Beck, E. Candell, R. Carr, F. Duncan, T. Forest, W. Korsch, J. W. Mark, R. D. McKeown, B. A. Mueller, and S. Wells, Nucl. Instrum. Methods Phys. Res., Sect. A **378**, 383 (1996).
[54]S. D. Covrig, E. J. Beise, R. Carr, K. K. Gustafsson, L. Hannelius, M. C. Herda, C. E. Jones, J. Liu, R. D. McKeown, R. Neveling, A. W. Rauf, and G. Smith, Nucl. Instr. and Meth. A **551**, 218 (2005).
[55]J. Gao, K. Gustafsson, R. Carr, C. E. Jones, R. D. McKeown, A. Scott, P. L. Anthony, R. F. Boyce, W. Burgess, A. Candia, W. Kaminskas, G. Oxoby, M. P. Racine, T. Weber, and J. G. Weisend II, Nucl. Instrum. Methods Phys. Res., Sect. A **498**, 90 (2003).
[56]I. Altarev, E. Schilling, S. Baunack, L. Capozza, J. Diefenbach, K. Grimm, T. Hammel, D. von Harrach, Y. Imai, E. M. Kabus, R. Kothe, J. H. Lee, A. Lopes Ginja, F. E. Maas, A. Sanchez-Lorente, G. Stephan, and C. Weinrich, Nucl. Instrum. Methods Phys. Res., Sect. A **564**, 13 (2006).
[57]J. A. Oyedele and A. A. Harms, Nucl. Instrum. Methods **167**, 255 (1979).
[58]A. A. Harms, S. Lo, and W. T. Hancox, J. Appl. Phys. **42**, 4080 (1971).
[59]J. C. Cook, Rev. Sci. Instrum. **80**, 023101 (2009).
[60]P. K. Kabir, G. Karl, and E. Obryk, Phys. Rev. D **10**, 1471 (1974).
[61]P. K. Kabir, Can. J. Phys. **53**, 2661 (1975).
[62]B. Ritchie, Phys. Rev. A **20**, 1915 (1979).
[63]M. Forte, Lett. Nuovo Cimento **34**, 296 (1982).
[64]M. Forte and C. E. Zeyen, Nucl. Instrum. Methods Phys. Res., Sect. A **284**, 147 (1989).
[65]V. L. Alexeev *et al.*, Nucl. Instrum. Methods Phys. Res., Sect. A **284**, 181 (1989).
[66]V. V. Fedorov *et al.*, Physica B **297**, 293 (2001).
[67]V. V. Voronin *et al.*, Appl. Phys. A **74**, 93 (2002).
[68]J. Byrne, *Neutrons, Nuclei, and Matter: An Exploration of the Physics of Slow Neutrons* (Institute of Physics Publishing, Bristol and Philadelphia, 1994).
[69]R. V. Jones, Proc. R. Soc. London, Ser. A **349**, 423 (1976).
[70]M. A. Player, Proc. R. Soc. London, Ser. A **349**, 441 (1976).
[71]G. Nienhuis, J. P. Woerdman, and I. Kuscer, Phys. Rev. A **46**, 7079 (1992).
[72]F. M. Piegsa and G. Pignol, Phys. Rev. Lett. **108**, 181801 (2012).
[73]E. G. Adelberger and T. A. Wagner, Phys. Rev. D **88**, 031101(R) (2013).
[74]F. Tasset, P. J. Brown, and J. B. Forsyth, J. Appl. Phys. **63**, 3606 (1988).
[75]E. Lelievre-Berna, P. J. Brown, and F. Tasset, Physica B **397**, 138 (2007).
[76]E. Lelievre-Berna, P. J. Brown, F. Tasset, K. Kakurai, M. Takeda, and L. P. Regnault, Physica B **397**, 120 (2007).
[77]V. V. Lukashevich, A. V. Aldushchenkov, and D. Dallman, Phys. Rev. C **83**, 035501 (2011).
[78]J. D. Bowman and V. Gudkov, Phys. Rev. C **90**, 065503 (2014).